RESEARCH ARTICLE

# Dedicated diffusion phantoms for the investigation of free water elimination and mapping: insights into the influence of $T_2$ relaxation properties

Ezequiel Farrher[1] | Farida Grinberg[1] | Li-Wei Kuo[2,3] | Kuan-Hung Cho[2] | Richard P. Buschbeck[1] | Ming-Jye Chen[2] | Husan-Han Chiang[2] | Chang-Hoon Choi[1] | N. Jon Shah[1,4,5,6]

[1]Institute of Neuroscience and Medicine 4, Medical Imaging Physics, Forschungszentrum Jülich, Jülich, Germany

[2]Institute of Biomedical Engineering and Nanomedicine, National Health Research Institutes, Miaoli, Taiwan

[3]Institute of Medical Device and Imaging, National Taiwan University College of Medicine, Taipei, Taiwan

[4]Department of Neurology, Faculty of Medicine, RWTH Aachen University, Aachen, Germany

[5]JARA BRAIN Translational Medicine, RWTH Aachen University, Aachen, Germany

[6]Institute of Neuroscience and Medicine 11, JARA, Forschungszentrum Jülich, Jülich, Germany

**Correspondence**
Ezequiel Farrher, Institute of Neuroscience and Medicine 4, Medical Imaging Physics, Forschungszentrum Jülich, Jülich, Germany.
Email: e.farrher@fz-juelich.de

Li-Wei Kuo, Institute of Biomedical Engineering and Nanomedicine, National Health Research Institutes, Miaoli, Taiwan.
Email: lwkuo@nhri.org.tw

Conventional diffusion-weighted (DW) MRI suffers from free water contamination due to the finite voxel size. The most common case of free water contamination occurs with cerebrospinal fluid (CSF) in voxels located at the CSF-tissue interface, such as at the ventricles in the human brain. Another case refers to intra-tissue free water as in vasogenic oedema. In order to avoid the bias in diffusion metrics, several multi-compartment methods have been introduced, which explicitly model the presence of a free water compartment. However, fitting multi-compartment models in DW MRI represents a well known ill conditioned problem. Although during the last decade great effort has been devoted to mitigating this estimation problem, the research field remains active.

The aim of this work is to introduce the design, characterise the NMR properties and demonstrate the use of two dedicated anisotropic diffusion fibre phantoms, useful for the study of free water elimination (FWE) and mapping models. In particular, we investigate the recently proposed FWE diffusion tensor imaging approach, which takes explicit account of differences in the transverse relaxation times between the free water and tissue compartments.

**KEYWORDS**
anisotropic diffusion fibre phantom, diffusion tensor imaging, free water elimination, free water mapping, multidimensional MRI, partial volume effect, transverse relaxation, variability

# 1 | INTRODUCTION

Diffusion-weighted (DW) MRI is a widely used, non-invasive technique for measuring water molecular diffusion in biological tissue.[2] The most common use of DW MRI in clinical practice is based on the observation of DW images without further processing. Due to its simplicity, diffusion tensor imaging (DTI) currently remains the most frequent method used for clinical analysis of DW MRI data.[3] During the last two decades, DTI metrics have been extensively used in the study of several neurodegenerative diseases,[4] brain neoplasms[5] and stroke,[6,7] as well as in studies relating to brain development and ageing.[8,9] DTI metrics can only be considered to be tissue specific if the voxel under analysis contains a single type of tissue. In cases when voxels contain more than one tissue type, DTI metrics integrate the microstructural characteristics of all tissue types within the voxel. This phenomenon is normally referred to as the partial volume effect (PVE), which is ubiquitous in DW MRI at conventional resolutions on clinical scanners ($2^3$–$3^3$ mm$^3$).[10,11] In particular, the PVE with cerebrospinal fluid (CSF) represents a serious limitation for DTI.

From the point of view of particle diffusion, CSF behaves as free water. That is, as water molecules do not experience restrictions, the apparent diffusion coefficient (ADC) is approximately equal to 3 μm$^2$/ms at 37°C, ie almost four times larger than the mean ADC observed in human brain tissue.[12] As a consequence, even small amounts of CSF within the voxel can strongly bias the tissue-specific DTI parameters. In particular, the ADC becomes elevated, whereas the corresponding fractional anisotropy (FA) is reduced.[10]

Free water contamination in DW MRI can happen in two ways. CSF surrounds the brain parenchyma and is also confined inside the ventricles. Therefore, DTI parameters for voxels located at the CSF-tissue interface will be affected. In this case, the PVE depends on the positioning of the imaging grid and also on the size of the structure under investigation.[13] Thus, small structures (eg the fornix) will be more affected by CSF contamination compared with larger structures.[14] Another type of free water contamination refers to the presence of intra-tissue water compartments sufficiently large to reflect free diffusivity, which has been observed, for example, in the case of vasogenic oedema.[15,16]

There are two kinds of approach for the reduction of free water contamination in DW MRI, namely, sequence based and model based. The most common sequence-based approach is FLAIR DW MRI.[17] This sequence makes use of the fact that the $T_1$ of CSF is longer than that of tissue, allowing one to choose an inversion-time such that the CSF signal is cancelled at the echo-time ($T_E$). However, this sequence suffers from a high specific absorption rate and longer acquisition times.[16] Another approach avoids an increase in acquisition time, compared with conventional settings,[18] by using shorter repetition times and a slice acquisition reordering to reduce the signal of the CSF. However, a common limitation of these sequences is the loss of signal-to-noise ratio compared with conventional settings (28% and 36%, respectively[18]).

The model-based approaches do not require a priori specially designed pulse sequences, but they do need to explicitly model the existence of a free water compartment within the voxel. Pierpaoli and Jones[15] initially noticed that vasogenic oedema and CSF have similar diffusion properties and therefore contribute to the total DW MRI signal in a similar manner. In order to obtain tissue-specific DTI parameters, they proposed the use of a two-compartment model, with one of the compartments referring to free water and the other to tissue. The free water compartment is characterised by isotropic, Gaussian diffusion with a diffusion coefficient equal to that of free water at the corresponding temperature, and the tissue compartment characterised by restricted diffusion, described by a diffusion tensor.[15,19] However the parameter estimation problem in two-compartment models is generally ill conditioned,[20,21] and in some circumstances ill posed.[16] In order to overcome this limitation, Pierpaoli and Jones proposed the acquisition of several diffusion weightings (b-values) in the range [0, 1.2] ms/μm$^2$. Although this approach mitigates the ill conditioned problem, it can greatly increase the acquisition time well beyond clinical constraints. Thus, several approaches have been proposed to optimize the b-values, the number of shells and the number of field gradient directions per shell, using simulations[21,22] or a minimization of the Cramér-Rao lower bound of the parameters of interest.[23,24]

Several works have also been devoted to avoiding the ill posed estimation problem in the case of single-shell experiments. Pasternak et al[16] initially proposed adding constraints to the model and a spatial regularization of the tissue diffusion tensor. This approach was shown to reduce the degeneracy of the estimation problem. However, it has been recently shown that such regularization does not fully cancel the degeneracy of the problem.[25] Another method using subject-based constraints in the mean (MD) or axial diffusivities showed some advantages for the investigation of small structures, such as the fornix, due to the lack of spatial regularization of the diffusion tensor.[14] So far, free water elimination (FWE) DTI models have been shown to reduce bias in DTI metrics and fibre tractography[13,14,19,26] and have also improved test–retest reproducibility.[27] Moreover, the free water volume fraction map has been shown to be a sensitive biomarker in vasogenic oedema[16] and neurodegenerative diseases such as dementia,[28] Alzheimer's disease[29] and Parkinson's disease.[30-32]

Although the aforementioned methods stabilize the parameter estimation problem, imposing these model assumptions leads to the risk of producing biased results. Recently, there has been a great effort to make the estimation problem well conditioned and to stabilize the solution without priors and regularizations.[23,24,33-35] In particular, it has been demonstrated that, due to the difference in the $T_2$ of free water and tissue, the addition of a $T_2$ attenuation term to each of the compartments and the use of different $T_E$ values leads to a more accurate, precise and robust estimation of the model parameters.[36] The underlying idea of this approach is inspired by the broadly studied multidimensional NMR methods used in the investigation of porous media and tissue.[37-42] However, there is a fundamental difference between the aforementioned correlation methods, which are based on the inversion of the Laplace transform, and the FWE model with explicit account of $T_2$ attenuation (FWET$_2$), in which the number of physical compartments is defined a priori.[36] Moreover, the difference in $T_2$ of the different compartments leads to a $T_E$ dependence of the relative free water fraction if the difference in $T_2$ is not explicitly modelled.[36,43]

Diffusion phantoms have become an indispensable tool for a broad set of applications, including the calibration of diffusion pulse sequences, the optimization of tractography algorithms and the validation of theoretical diffusion models, data post-processing techniques and numerical simulations. Existing phantoms with independently known diffusion properties are based on simple liquids[44] or liquid solutions/mixtures[45] that are useful for the calibration of field gradients, for quality assurance of various scanner conditions, for inter-scanner reproducibility etc. However, these phantoms are too simplistic and do not reflect most features of diffusion in brain tissue. On the other hand, when the complexity of a phantom microstructure is increased in order to match it to the enormous complexity of in vivo brain tissue, the possibility of deriving its diffusion and relaxation properties based on the microstructural properties decreases. Thus, although the terms "gold standard" or "ground truth" are often used in the jargon,[46,47] they refer rather to the possibility of verifying specific features of interest addressed by the suggested models/methods under investigation, while the lack of "true" gold standard phantoms is generally recognized by the community.[48,49] The requirements of physical phantoms, therefore, mostly relate to the needs of a specific problem and should fulfil the following criteria[46]:

a. exhibits the microstructural property of interest affecting the measured signal;
b. is well characterised in terms of its microstructural properties;
c. is easy to assemble and reproducible;
d. is stable and non-toxic.

An excellent discussion on this topic can be found in a recent review by Fieremans and Lee.[46]

Given the great attention that FWE has gained during recent years, here we aim to introduce the design of two artificial, anisotropic diffusion fibre phantoms and to characterise their NMR properties in the framework of FWE models. In particular, we investigate the recently introduced FWET$_2$.[36] One of the phantoms is designed to mimic the first case of free water contamination described here, ie voxels at the CSF-tissue interface. This phantom contains sections of different thicknesses of parallel fibre bundles, separated by compartments of free water of different sizes. The second phantom is based on our previously published prototype[50] and is intended to mimic the situation of PVE with intra-tissue free water compartments. The phantoms were constructed using Dyneema polyethylene fibres (SK75 dtex1760, DSM, Geleen, The Netherlands), which have been shown to be useful in mimicking some features of water diffusion in brain white matter.[51-56] Given the highly complex process of deriving ground truth parameters based on microstructural features, we instead construct "reference truth" maps of the model parameters using the median of each parameter of interest, taken over several scan sessions acquired at two different sites. Therefore, in order to ensure the stability of the phantoms, we first investigate the variability of both intra-site (several experiments at a single site) and inter-site (experiments at two sites) model parameters.[1]

We expect our prototypes to benefit the design and optimization of experimental protocols for DW MRI, as well as the development of data pre- and post-processing methodologies.

## 2 | THEORY

Within the diffusion tensor distribution (DTD) framework,[57] the MRI signal can be regarded as the result of the contribution of several domains characterised by a transverse relaxation time $T_2$ and a diffusion tensor $\mathbf{D}$ (we neglect longitudinal relaxation effects throughout this work). The total MRI signal is thus expressed in terms of the distribution $P(T_2, \mathbf{D})$ and the response kernel $K(T_E, \mathbf{b}, T_2, \mathbf{D})$, according to[58]

$$S(T_E, \mathbf{b}) = S_0 \int_0^\infty \int_\Omega P(T_2, \mathbf{D}) K(T_E, \mathbf{b}, T_2, \mathbf{D}) \mathrm{d}\mathbf{D} \, \mathrm{d}T_2, \tag{1}$$

where $S_0$ is the proton signal, $\mathbf{b}$ is the diffusion encoding tensor[59] and $\Omega$ is the integration domain for $\mathbf{D}$. For the case of anisotropic, Gaussian diffusion, the response kernel is given by $K(T_E, \mathbf{b}, T_2, \mathbf{D}) = \exp(-T_E/T_2)\exp(-\mathbf{b}:\mathbf{D})$, where $\mathbf{b}:\mathbf{D} \equiv \sum_{ij} b_{ij}D_{ij}$ denotes the generalized scalar product.

### 2.1 | FWE DTI

Conventional FWE DTI is based on a two-compartment model in the slow-exchange limit. The signal for the free water compartment is modelled as an isotropic, Gaussian diffusion signal, whereas the signal for the tissue compartment is described by an anisotropic, DTI-like signal.[15,16] The total signal within the voxel is written as follows:

$$S(b, \mathbf{n}) = S_0' \left[ f e^{-bD_w} + (1-f) e^{-b\mathbf{n}^\mathsf{T}\mathbf{D}_t\mathbf{n}} \right], \tag{2}$$

where $S_0' = S_0 \exp(-T_E/T_2)$ is the $T_2$-weighted (T$_2$W) proton signal, $f$ and $D_w$ are the relative fraction and diffusion coefficient for the free water compartment and $\mathbf{D_t}$ is the second-rank symmetric, positive-definite diffusion tensor for the tissue compartment. The fraction $f$ in the case of compartments with different transverse relaxation times depends on the echo-time, $T_E$ (see below). Within the DTD framework, this model is equivalent to having a distribution $P(T_2, \mathbf{D}) = \delta(T_2' - T_2)[f\delta(\mathbf{D} - D_w\mathbf{I}) + (1 - f)\delta(\mathbf{D} - \mathbf{D_t})]$ in Equation 1, where $\delta(...)$ is the Dirac delta function and $\mathbf{I}$ is the identity matrix. The experimentally controlled parameters are the strength and direction of the diffusion weightings, $b = \mathrm{Tr}(\mathbf{b})$[57] and $\mathbf{n} = (n_x, n_y, n_z)^\mathrm{T}$, respectively.

## 2.2 | DTI with explicit $T_2$ attenuation

Assuming a voxel containing a single tissue type, the simplest representation of the DW and T$_2$W MRI signal is written as follows:

$$S(T_E, b, \mathbf{n}) = S_0\, e^{-\frac{T_E}{T_2}}\, e^{-b\mathbf{n}^\mathrm{T}\mathbf{D}\mathbf{n}}, \tag{3}$$

where $T_2$ is the transverse relaxation time.[12] Notice that Equation 3 merely represents the DTI signal with an explicit $T_2$ exponential attenuation. We shall refer to this approach through this work as DTIT$_2$.

## 2.3 | FWE DTI with explicit $T_2$ attenuation

The FWET$_2$ model assumes that the DW and T$_2$W MRI signal originates from two compartments with different transverse relaxation times and diffusion properties, in the slow-exchange regime.[36] In this case, the signal is written as follows:

$$S(T_E, b, \mathbf{n}) = S_0\left[f_w\, e^{-\frac{T_E}{T_{2,w}}}\, e^{-bD_w} + (1 - f_w)e^{-\frac{T_E}{T_{2,t}}}\, e^{-b\mathbf{n}^\mathrm{T}\mathbf{D_t}\mathbf{n}}\right], \tag{4}$$

where $T_{2,w}$ and $T_{2,t}$ denote the transverse relaxation times for the free water and tissue compartments, respectively, and $f_w$ is the true, $T_E$-independent relative water fraction, which is related to the $T_E$-dependent relative free water fraction, $f(T_E)$, according to[16,36,43,60]

$$f(T_E) = \frac{f_w\, e^{-\frac{T_E}{T_{2,w}}}}{f_w\, e^{-\frac{T_E}{T_{2,w}}} + (1 - f_w)e^{-\frac{T_E}{T_{2,t}}}}. \tag{5}$$

Note that, within the DTD framework, the FWET$_2$ model is equivalent to having a distribution $P(T_2, \mathbf{D}) = f_w\delta(T_2 - T_{2,w})\delta(\mathbf{D} - D_w\mathbf{I}) + (1 - f_w)\delta(T_2 - T_{2,t})\delta(\mathbf{D} - \mathbf{D_t})$ in Equation 1.

# 3 | MATERIALS AND METHODS

## 3.1 | Anisotropic diffusion phantoms

Both phantoms utilized in this work were constructed using Dyneema polyethylene fibres (solid fibres—ie not hollow— ~8 μm in radius) wound on Perspex platforms, and were submerged in a cylindrical container with distilled water.[50,51] Dyneema can be found in bundles of approximately 700 single fibre strands. The bulk water contained 15 mg of NaN$_3$ as a preservative (0.001% w/v). Both phantoms were positioned together inside the container so that they could be measured simultaneously.

### 3.1.1 | Phantom 1

This phantom contains five sections of parallel fibre bundles of different thicknesses $d$ = 2, 4, 6, 8 and 10 mm and a height of 10 mm, separated by alternating compartments of free water and Perspex material (see Figure 1A). Based on the construction characteristics, the
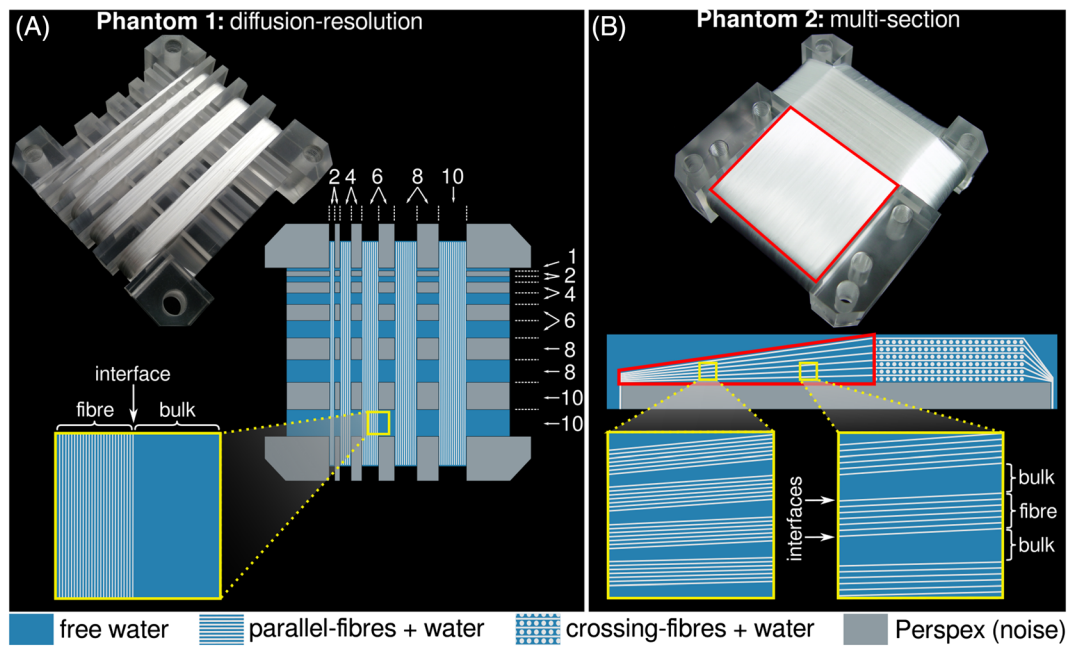
**FIGURE 1** Photographs and schemes of the phantoms. A, phantom 1. Diffusion-resolution phantom with five sections of bundles of parallel fibres of increasing thickness from left to right, and a height of 10 mm. The sections of fibres are separated by alternating compartments of free water and Perspex of increasing sizes (from top to bottom). The numbers in the picture indicate the dimensions in millimetres. B, phantom 2. Multi-section phantom containing four sections with different fibre configurations.[50] The section of interest for this work (red ROI) consists of nearly parallel fibre layers, which go from an area of high packing density (left-hand side) to an area of low packing density (right-hand side). In addition, the phantom contains two sections with fibres crossing at right angles and spatially constant volume fraction, and one section of parallel fibres with spatially constant volume fraction. These two fibre configurations are not considered in this work

fibre volume fraction on the length-scale of a typical voxel size is expected to be homogeneous. Thus, depending on the position of the imaging grid and voxel size, one can generate data sets with different degrees of PVE. A similar phantom has been published in the literature, ie containing sections of fibre bundles of different thicknesses.[11] In contrast to the cylindrical design of the phantom in Reference 11, the sections of fibre bundles in our design are straight and can, therefore, be positioned at a given angle with respect to the external magnetic field. This, in turn, enables the susceptibility-induced, background gradients to be controlled.[61]

### 3.1.2 | Phantom 2

This is a multi-section phantom, similar to the one published in our previous work[50] (Figure 1B). This phantom was constructed by stacking layers of fibres in alternating directions, crossing at right angles. The thickness of each layer lies in the range from approximately 180 μm to 220 μm. As a result of this configuration, a free water compartment of planar structure between the layers with increasing volume is formed (from left to right in Figure 1B). Therefore, several compartments will be present within a voxel, thus producing the desired intra-tract PVE free water contamination.

### 3.2 | MRI experiments

Experiments were performed with a 3 T Siemens Prisma scanner (Siemens, Erlangen, Germany) and a 64-channel receive coil provided by the manufacturer. A 2D DW spin-echo pulse sequence with monopolar pulse field gradients and EPI readout was used. Two types of experiment were performed: DW and $T_2$W, both using coronal slices. The protocol parameters for the DW experiment were $T_E$ = 70 ms, repetition time, $T_R$ = 6.9 s, $b$ = 0 (eight repetitions), 0.4 (21 gradient directions) and 1.0 (35 gradient directions) ms/μm$^2$. The $T_2$W experiment was performed for 10 values of $T_E$ = 70, 90, 110, 130, 150, 200, 250, 300, 350 and 400 ms and $T_R$ = 22 s (and $b$ = 0 ms/μm$^2$). Other parameters were voxel size = $2^3$ mm$^3$, matrix size = 96 × 96 × 50, number of averages 5 and bandwidth 1580 Hz/pixel.

For the analysis of intra- and inter-site variability, the former protocol was performed on the same phantom three times at "Site 1" and three times at "Site 2". Both sites were equipped with a 3 T Siemens Prisma scanner. The Syngo software version at Site 1 was VD13, whereas at Site 2 it was VE11. The time difference of each measurement, as referenced to the first measurement at Site 1, was 435 days (Site 1, Time Point 2), 495 days (Site 1, Time Point 3), 526 days (Site 2, Time Point 1), 540 days (Site 2, Time Point 2) and 564 days (Site 2, Time Point 3).

## 3.3 | Model parameter estimation

All images were processed using in-house MATLAB scripts (MATLAB 2015a, MathWorks, Natick, MA, USA). In order to avoid a $T_1$ modulation of the signal due to different $T_R$ values between the two experiments, we normalized the signal of the $T_2W$ experiment, $S_{T_2W}(T_E)$, as $S_{norm}(T_E) = S_{T_2W}(T_E)S_{DW}(b=0)/S_{T_2W}(T_{E,1})$, for 70 ms ≤ $T_E$ ≤ 400 ms, where $T_{E,1}$ = 70 ms and $S_{DW}(b)$ is the signal of the DW experiment. $FWET_2$ model (Equation 4) parameter estimation was performed using the whole experimental data set simultaneously. Additionally, estimation of FWE model parameters (Equation 2), using only the DW experiment, was performed for the sake of comparison (see Section 4.4).

$FWET_2$ parameter estimation was performed in two steps.

i. In the first step, $DTIT_2$ model parameters were estimated by fitting Equation 3 to the whole experimental data set (DW and $T_2W$), in order to generate an initial guess for $T_{2,t}$ and $\mathbf{D}_t$. Additionally, $DTIT_2$ parameters in the bulk area of the phantom were used to assess $T_{2,w}$ and $D_w$. The estimation of $DTIT_2$ parameters was performed via weighted linear least squares (WLLS).[62] The WLLS estimator for the $DTIT_2$ model parameters, $\boldsymbol{\theta}_{DTIT_2} = [\ln S_0, D_{11}, D_{12}, D_{13}, D_{22}, D_{23}, D_{33}, 1/T_2]^T$, is written as follows:

$$\hat{\boldsymbol{\theta}}_{DTIT_2} = \left(\mathbf{X}^T \mathbf{w} \mathbf{X}\right)^{-1} \mathbf{X}^T \mathbf{w} \mathbf{y}, \tag{6}$$

where $\mathbf{y}$ ($N \times 1$) is a column vector whose elements are given by the natural logarithm of the $N$ measured signals, ie $y_i = \ln S_i$ ($i = 1,...,N$), and the weighting matrix, $\mathbf{w}$ ($N \times N$), is a diagonal matrix whose elements are given by $w_{i,i} = S_i^2$. The $i$th row of the design matrix, $\mathbf{X}$ ($N \times 8$), is written as $X_{i,:} = \left[1, -b_i n_{ix}^2, -2b_i n_{ix} n_{iy}, -2b_i n_{ix} n_{iz}, -b_i n_{iy}^2, -2b_i n_{iy} n_{iz}, -b_i n_{iz}^2, -T_{E,i}\right]$.

ii. In the second step, $FWET_2$ model parameters, $\boldsymbol{\theta}_{FWET_2} = [S_0, f_w, D_{11}, D_{12}, D_{13}, D_{22}, D_{23}, D_{33}, T_{2,t}]^T$, were estimated via constrained non-linear minimization of the least-squares estimator, which is written as follows:

$$\hat{\boldsymbol{\theta}}_{FWET_2} = \arg \min_{\boldsymbol{\theta}_{FWET_2}} \sum_{i=1}^{N} [S_i - S[\boldsymbol{\theta}_{FWET_2}]]^2, \tag{7}$$

where $S(\boldsymbol{\theta}_{FWET_2})$ is the signal model. The minimization of Equation 7 was performed using the function `fmincon` available in MATLAB using the `interior-point` algorithm, subject to the following linear and non-linear constraints:

a. linear constraints, $0 \leq f_w \leq 1$ and $T_{2,t} \leq T_{2,w}$
b. non-linear constraints, $0 < \lambda_k \leq D_w$ ($k$ = 1,2,3), where $\lambda_k$ denotes the eigenvalues of the tissue diffusion tensor $\mathbf{D}_t$ ($\lambda_1 \geq \lambda_2 \geq \lambda_3$).[63]

The minimization process in this step was initialized using the values of $T_2$ and $\mathbf{D}$ generated in Step (i) and $f_w$ = 0.1. The free water parameters, $D_w$ and $T_{2,w}$, estimated in Step (i) in the bulk of the phantoms were fixed during minimization.

FWE model parameter estimation was also carried out following Steps (i) and (ii), with the exception that, in this case, the parameters were estimated using only the DW data set.

DTI parameters FA, MD and radial diffusivity (RD) were evaluated for each case based on the corresponding diffusion tensor as described elsewhere.[64] In the case of voxels containing only free water ($f_w$ = 1), the tissue diffusion tensor can erroneously fit the signal from the free water compartment. In this case, given that both the free water and the tissue compartment can fit the total signal equally well, the free water fraction can take any value between 0 and 1, as explained in References 21 and 22. Therefore, the analysis of voxels for which $f_w \geq 0.95$, $\lambda_{2,3} \geq 2.0 \mu m^2$/ms or $T_{2,t} \geq 2.4$ s was skipped.

## 3.4 | Proton density and fibre volume fraction

In order to assess the relative proton density, PD, we first computed the intensity bias field from the parameter $S_0$ in Equation 4 following the method in Reference [65]. Then $S_0$ was normalized using the calculated intensity bias field (so that PD = 1 in the bulk). The fibre volume fraction, $\phi$, in the case of a voxel containing a single compartment is simply given by $\phi = 1 - PD$. However, if the voxel contains a free water compartment with a relative fraction $f_w$, as described by Equation 4, the true fibre volume fraction at the fibre compartment can be shown to be

$$\phi = \frac{1 - PD}{1 - f_w PD} \tag{8}$$

provided that $f_w < 1$ (Figure 4E).

## 3.5 | Reference truth maps and intra- and inter-site variability

Reference truth $DTIT_2$ and $FWET_2$ model parameter maps were constructed by taking the voxel-wise median of all time points and sites. On the other hand, voxel-wise deviation maps were assessed via the interquartile range, ie the distance between the first and the third quartile. The main underlying assumption of this approach for constructing reference truth maps, which integrates information from experiments from different sites, is that the inter-site variability is negligible and the main contribution to between-sessions variations is of intra-site nature. In other words, there is no site bias.[1] This will be discussed in detail in Subsection 5.3 in the context of the current results.

Variability of $DTIT_2$ and $FWET_2$ model parameters, both intra- and inter-site, was investigated following the framework proposed by Walker et al.[1] It assumes that experiments have been performed at $p = 1, ..., P$ sites and $q = 1, ..., Q_p$ time points (here $P = 2$ and $Q_p = 3$ for $p = 1, 2$; see Appendix A for details) and includes the following steps.

i. Outlier identification for all $DTIT_2$ and $FWET_2$ parameter maps by subtracting a given map at site $p$ and time point $q$, from the corresponding median taken over all sites and scan sessions. Significant deviations from the median are considered to be outliers.

ii. Evaluation of intra- and inter-site variability maps, $\sigma_{intra}$ and $\sigma_{inter}$ (Equations A1, A2), as well as the intra- and inter-class correlation coefficients, $ICC_{intra}$ and $ICC_{inter}$ (Equations A3, A4), for all model parameters.

Before the analysis of variability was performed, all $FA_{p,q}$ maps from $DTIT_2$ were coregistered to $FA_{1,1}$ (Site 1, Scan Session 1) with the help of the toolkit FLIRT available in FSL,[66,67] using the rigid body model. The resulting transformation matrix was subsequently applied to the remaining parameter maps.

It should be noted that, in order to avoid any site and/or scan session bias in MD and $T_2$ maps due to possible differences in the room temperature, we normalized each of these maps by the corresponding bulk value of each scan session, before the variability analysis and the construction of reference truth maps.

## 4 | RESULTS

## 4.1 | Phantom 1

Figure 2 summarizes the results for Phantom 1 for both the single scan (Figure 2A-C) and reference truth (Figure 2D-F) cases. The maps of MD, FA and $T_2$ from $DTIT_2$ (Figure 2A and 2D) are compared with the corresponding maps from $FWET_2$ (Figure 2B and 2E). A first glance at the maps suggests that $DTIT_2$ parameters in voxels located at the edge of the sections of fibre bundles, where the $f_w$ values are higher, are affected by PVE. In particular, the leftmost section, which is 2 mm thick, is hardly visible in the $DTIT_2$ FA map (yellow arrows in Figure 2A and 2D). However, the PVE with free water in the parameters can be reduced when the $FWET_2$ model is used. See, for instance, the yellow arrow in Figure 2B and 2E, where the diffusion properties for the same section appear more similar to those voxels unaffected by PVE. Note that voxels containing only free water were not analysed with $FWET_2$ and are displayed in black (see Subsection 3.3).

The profiles of MD, FA, $T_2$ and $f_w$ taken along the blue, horizontal line indicated in Figure 2B are shown in Figure 2C (single session) and 2F (reference truth), for the $DTIT_2$ (green line) and $FWET_2$ (orange line) parameters. Grey zones represent voxels located at the
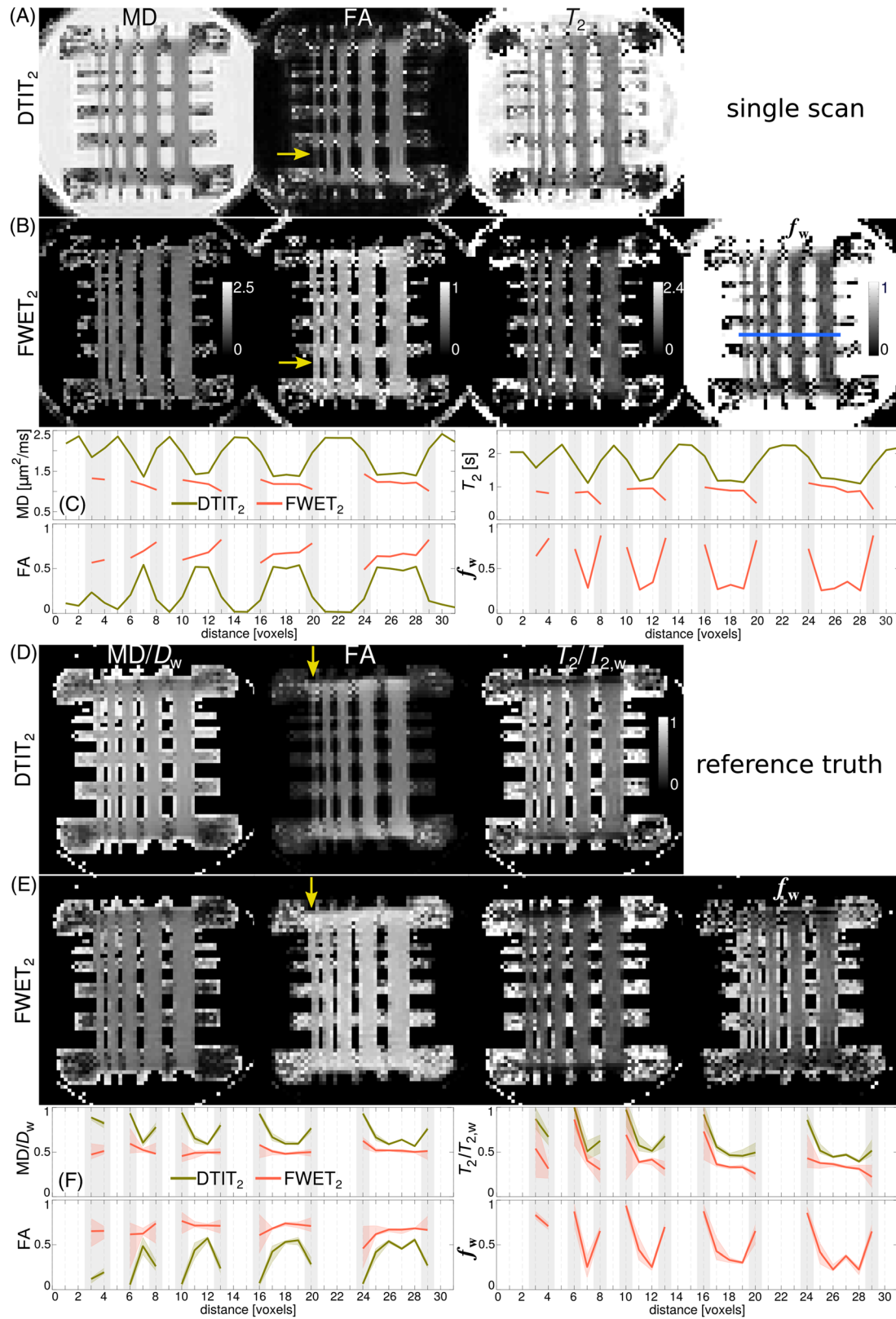
**FIGURE 2** A, D, maps of MD, FA and $T_2$ from DTIT$_2$; B, E, maps of MD, FA, $T_{2,t}$ and $f_w$ from FWET$_2$; C, F, profiles of MD, FA, $T_2$ and $f_w$ taken along the blue line. Both single scan (A-C) and reference truth (D-F) are shown. Grey areas denote voxels located at the bulk-fibre interface. Bulk diffusivity and transverse relaxation time were $D_w = (2.30 \pm 0.02)$ μm$^2$/ms and $T_{2,w} = (2.42 \pm 0.16)$ s, respectively. For the construction of reference truth maps (D, E), MD and $T_2$ maps were normalized to the corresponding bulk value of each scan session, so as to avoid any bias due to possible differences in the room temperature. Voxels where $f_w \geq 0.95$, $\lambda_{2,3} \geq 2.0$μm$^2$/ms or $T_{2,t} \geq 2.4$ s (ie bulk water) were not considered in the analysis and are therefore not displayed for FWET$_2$

interface between the section of fibres and the bulk water. The presence of a relative fraction of free water strongly affects the estimated diffusion and relaxation properties of the section of fibres. However, FWET$_2$ allows the PVE in these parameters to be reduced, given that a more constant profile is expected, based on the homogeneity of the fibre volume fraction in the length-scale of the sections of fibre bundles. Therefore, any major change in the diffusion or relaxation characteristics is expected to be due to free water contamination.

It is worth mentioning that, in the construction of the reference truth maps and the corresponding profiles, those voxels located at the interface between the bulk water and sections of fibre bundles reflect not only variations due to the intrinsic noise of the imaging protocol and the phantom itself, but also variations introduced by the position of the imaging grid, which changes from session to session in a random manner and therefore increases the parameters' variability.

## 4.2 | Phantom 2

Figure 3 summarizes the results for the multi-section phantom for both single scan (Figure 3A-C) and reference truth (Figure 3D-F) cases. The maps of MD, FA and $T_2$ from DTIT$_2$ (Figure 3A and 3D) are compared with the corresponding maps from FWET$_2$ (Figure 3B and 3E). All maps from DTIT$_2$ show an intensity change from left to right in the region of interest (ROI) demarked by the blue rectangle in Figure 3A. That is, MD and $T_2$ increase, whereas FA decreases. However, these changes become less pronounced in the corresponding maps from FWET$_2$. In particular, the transverse relaxation time in the fibre compartment is visually constant, within the large standard deviation of this parameter (see grey shaded areas in Figure 3C).

In order to better visualize these changes, we evaluated spatial profiles for each map, shown in Figure 3C (single session) and 3F (reference truth), for the DTIT$_2$ (green) and FWET$_2$ (orange) parameters. The abscissas refer to the horizontal position in the blue ROI. Solid lines and grey, shaded areas in Figure 3C denote the mean and standard deviation of a given parameter taken along a vertical stripe in the blue ROI (where $f_w$ was observed to be approximately constant). Thus the grey, shaded areas in Figure 3C show the variations of a given parameter along each vertical stripe in the blue ROI. In contrast, solid lines and coloured, shaded areas in Figure 3F correspond to the mean along a vertical stripe in the blue ROI of the first quartile map (lower line of the coloured, shaded area), median map (central line) and third quartile map (upper line). Therefore, in this case, the colour-shaded areas in Figure 3F denote the variations of the phantom parameters across the six scan sessions. A comparison of the profiles of DTIT$_2$ versus FWET$_2$ parameters demonstrates that a change in $f_w$ is accompanied by changes in DTIT$_2$ metrics. However, these changes are less pronounced when FWET$_2$ is used. The change in MD and FA from FWET$_2$ (Figure 3B and 3E), which allows one to more accurately assess the diffusion and relaxation properties of the fibre compartment, suggests that there is a decrease in the fibre volume fraction of the fibre compartment (from left to right). However, this change in the fibre volume fraction does not produce a significant change in $T_{2,t}$ (Figure 3C and 3F). Therefore, the observed change in $T_2$ from DTIT$_2$ is mainly due to the increase in the size of the free water compartment. This feature is further analysed in the following subsection.

## 4.3 | Proton density and fibre volume fraction

Figure 4 illustrates the maps of PD and $\phi$ (calculated following Equation 8), for Phantom 1 (Figure 4A) and Phantom 2 (Figure 4C) and both single scan (top) and reference truth cases (bottom).

In the case of Phantom 1, voxels at the interface between the bulk and sections of fibre bundles show increased values of PD compared with voxels unaffected by PVE. Conversely, the maps of $\phi$ are more spatially homogeneous across the sections of fibres. This is demonstrated by the profiles of PD (orange line), $f_w$ (blue line) and $\phi$ (grey line) shown in Figure 4B for the single scan (top) and reference truth (bottom). All voxels located at the edge of the sections of fibres show higher PD and $f_w$ values, compared with voxels unaffected by PVE. Moreover, the profiles of $\phi$ have a rather flat appearance, corresponding to the expected spatial homogeneity of the fibre volume fraction.

In Phantom 2, the spatial change in the size of the free water compartment corresponds to an increase of PD (from left to right in the blue ROI in Figure 4C) and a slight decrease of $\phi$. This is clearly shown in the profiles plotted in Figure 4D for PD (orange), $f_w$ (blue) and $\phi$ (grey). The increase in $f_w$ is accompanied by an increase in the total PD, whereas a decrease of approximately 7% (0.78 to 0.73) is observed in $\phi$. Although the change in $\phi$ is rather small, it is seemingly enough to induce changes in the diffusion properties, as shown in Figure 3C and 3F, but not observable changes in $T_{2,t}$. For a quantitative comparison, RD/$D_w$ and FA from FWET$_2$ (ie in the fibre compartment) are plotted against $\phi$ in Figure 5A and 5B. Additionally, the theoretical predictions for the RD in a system of parallel cylinders in the long-time limit (Equations B1-B3) under different conditions of fibre volume fractions and packing geometries (square and hexagonal lattices, see Appendix B for details) are also plotted. One can see that, although the arrangement of the fibres in the phantom follows neither the square nor the hexagonal lattices but is rather random, the
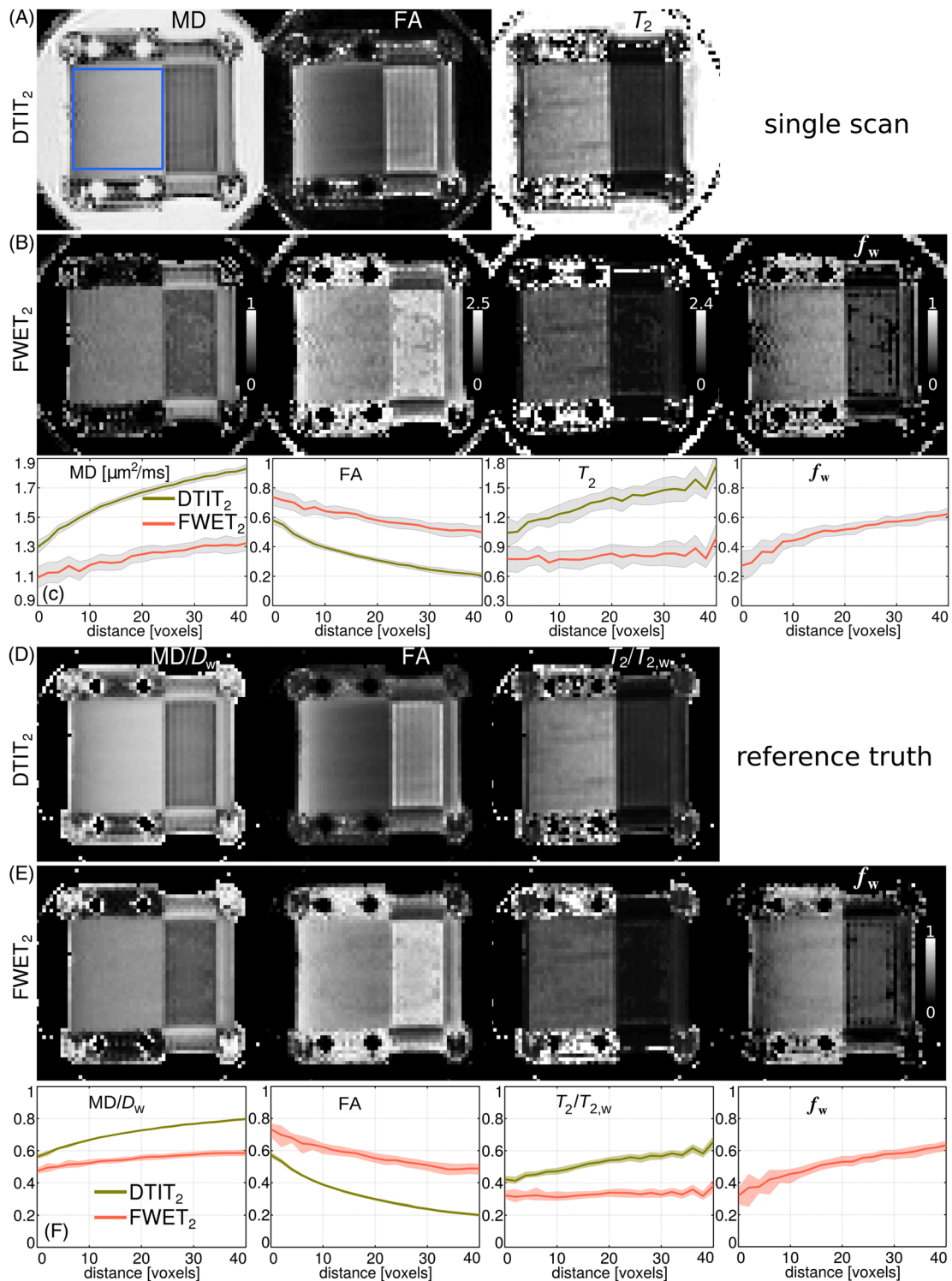
**FIGURE 3**  A, D, maps of MD, FA and $T_2$ from DTIT$_2$; B, E, maps of MD, FA, $T_{2,t}$ and $f_w$ from FWET$_2$; C, F, spatial profiles for MD, FA, $T_2$ and $f_w$ from DTIT$_2$ and FWET$_2$. Both single scan (A-C) and reference truth (D-F) are shown. In the profiles (C, F), the abscissas refer to a horizontal position in the blue ROI (A). Solid lines and grey, shaded areas in C denote the mean and standard deviation of a given parameter taken along a vertical stripe in the blue ROI. Solid lines and coloured, shaded areas in F denote the mean along a vertical stripe in the blue ROI of the first quartile map (lower line of the coloured, shaded area), median map (central line) and third quartile map (upper line). Bulk water diffusivity and transverse relaxation time were $D_w$ = (2.30 ± 0.02) μm$^2$/ms and $T_{2,w}$ = (2.60 ± 0.15) s, respectively. For the construction of reference truth maps (D, E), MD and $T_2$ maps were normalized to the corresponding bulk value of each scan session, so as to avoid any bias due to possible differences in the room temperature. Voxels where $f_w$ ≥ 0.95, $\lambda_{2,3}$ ≥ 2.0 μm$^2$/ms or $T_{2,t}$ ≥ 2.4 s (ie bulk water) were not considered in the analysis and are therefore not displayed (see Subsection 3.3). The artefact observed in the left-hand side of the blue ROI is the result of a field distortion due to a remaining air bubble trapped between the fibres
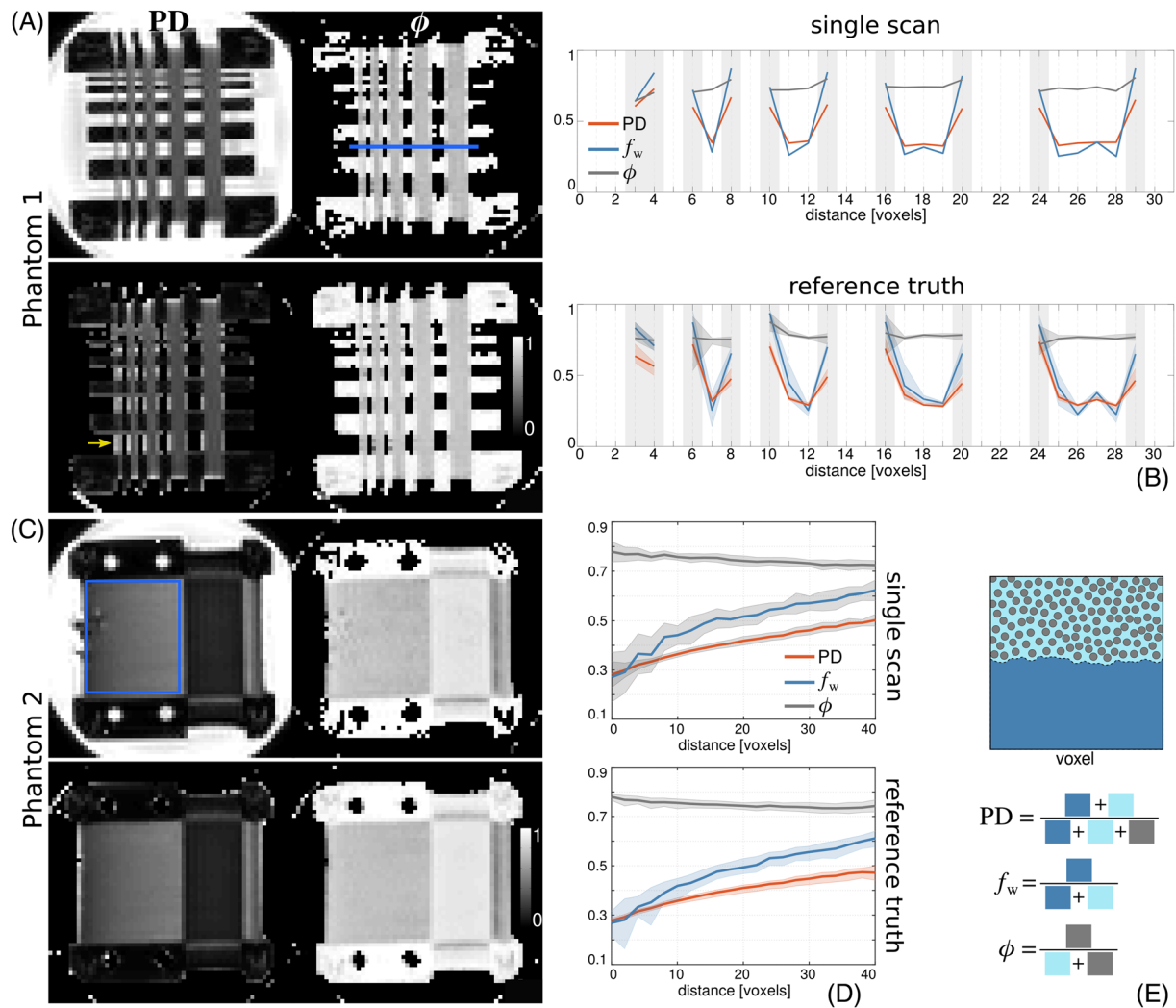
**FIGURE 4** A, C, maps of the PD and fibre volume fraction in the fibre compartment, $\phi$ (equation 8), for Phantom 1 (A) and Phantom 2 (C). Both a single scan session (top) and reference truth (bottom) are shown. B, D, spatial profiles for PD, $f_w$ and $\phi$ for Phantom 1 (B) and Phantom 2 (D). Both a single scan session (top) and reference truth (bottom) are shown. The abscissas refer to a horizontal position in the blue ROI (A). Solid lines and shaded areas in D (top) denote the mean and standard deviation of a given parameter taken along a vertical stripe in the blue ROI. Solid lines and coloured, shaded areas in D (bottom) denote the mean along a vertical stripe in the blue ROI of the first quartile map (lower line of the coloured, shaded area), median map (central line) and third quartile map (upper line). E, pictorial explanation of the meaning of each parameter. Grey colour refers to fibres, whereas light blue and dark blue refer to water in the restricted and free water compartments, respectively

trend for RD/$D_w$ and FA is clearly in the same direction as the theoretical prediction, as it reflects an abrupt decrease when approaching the close packing conditions.

## 4.4 | $f$ versus $f_w$

In order to evaluate the effects of accounting for differences in the transverse relaxation times between the water and fibre compartments on the estimation of the free water fraction, we exploit the fact that we have access to a range of free water volume fractions in Phantom 2 and plot $f$ from FWE (Equation 2) versus $f_w$ from FWET$_2$ (Equation 4). The map of $f_w$ was used to cluster the voxels in the blue ROI (Figure 3A) into eight equally spaced bins in the range [0.05, 0.7]. The mean and standard deviation of $f$ and $f_w$ were calculated within these bins and plotted in Figure 6 (orange circles). Equation 5 is also plotted for comparison (orange line) using $T_E$ = 70 ms and the estimated mean transverse relaxation times for the bulk compartment, $T_{2,w}$ = (2.53 ± 0.15) s, and fibre compartment, $T_{2,t}$ = (0.77 ± 0.08) s. One can see that $f$ is slightly larger than $f_w$ in the whole range (see the dashed, black line denoting the identity line). For the sake of comparison, Equation 5 was plotted using the same values of $T_{2,w}$ and $T_{2,t}$ and $T_E$ = 500 ms (blue curve). The difference in this case becomes larger. Finally, Equation 5 was plotted using literature values for the
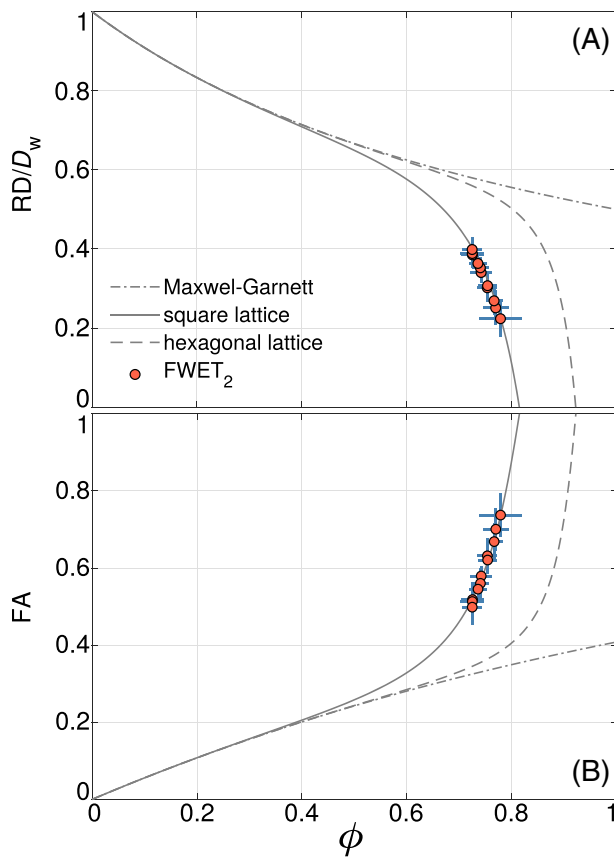
**FIGURE 5** RD (from FWET$_2$), relative to the bulk diffusivity, $D_w$ (A), and FA (from FWET$_2$) (B) versus fibre volume fraction $\phi$. Orange circles and blue bars denote the mean and standard deviation, respectively. Theoretical predictions (Appendix B) are shown for the sake of comparison using equation B1 (dotted-dashed lines), equation B2 (solid lines) and equation B3 (dashed lines)

transverse relaxation times for in vivo brain CSF, $T_{2,w}$ = 500 ms,[68] and tissue, $T_{2,t}$ = 60 ms at 3 T,[69] and $T_E$ = 80 ms. In this case, $f$ can be up to 75% larger than $f_w$.

## 4.5 | Inter-site and intra-site variability

The outlier identification step did not reveal outliers in any of the six scans (see Supplementary Figure S1). Figure 7 summarizes the intra- and inter-site variability maps, $\sigma_{intra}$ and $\sigma_{inter}$ (Equations A1 and A2), as well as ICC$_{intra}$ and ICC$_{inter}$ maps (Equations A3 and A4), for all DTIT$_2$ and FWET$_2$ parameters. All intra-site variability maps show significantly higher intensity values than the inter-site ones. This behaviour is more pronounced in the ICC parameters, where ICC$_{intra}$ shows much higher values than ICC$_{inter}$. In the case of Phantom 1, one can also observe that both variability values are higher in voxels located at the edge of the sections of fibre (red arrows) compared with those voxels unaffected by PVE. This is not the case in Phantom 2, where both variability and ICC parameters show a fairly homogeneous distribution in the blue ROI.

## 5 | DISCUSSION

In this work, we introduced the design, and demonstrated the use, of two anisotropic, diffusion fibre phantoms for the investigation of FWE models. In particular, we investigated the recently introduced FWE DTI model, which explicitly takes into account differences in the transverse relaxation times between compartments (FWET$_2$). Our phantoms fulfil the four criteria described in Section 1, as follows.

a. 'Exhibit the microstructural property of interest affecting the measured signal'. The effect of both types of free water contamination on the DW and T$_2$W signal described in Section 1 was successfully mimicked. The diffusion-resolution phantom (Phantom 1, Figure 1A) was designed to mimic the PVE occurring in voxels at the CSF-tissue interface. The multi-section phantom (Phantom 2, Figure 1B), on the other hand, was

**FIGURE 6** Orange circles and light blue bars depict the mean and standard deviation of $f$ from FWE (equation 2) versus $f_w$ from FWET$_2$ (equation 4), calculated using a clustered mask based on the map of $f_w$, using eight equally spaced bins in the range [0.05, 0.7]. Equation 5 is plotted for comparison using $T_E = 70$ ms and $T_E = 500$ ms and the mean transverse relaxation times for the bulk $T_{2,w} = (2.53 \pm 0.15)$ s and fibre $T_{2,t} = (0.76 \pm 0.10)$ s. for the sake of comparison, equation 5 is shown using literature values of the transverse relaxation times for in vivo brain CSF, $T_{2,w} = 500$ ms,[68] and tissue, $T_{2,t} = 60$ ms at 3 T,[69] and $T_E = 80$ ms
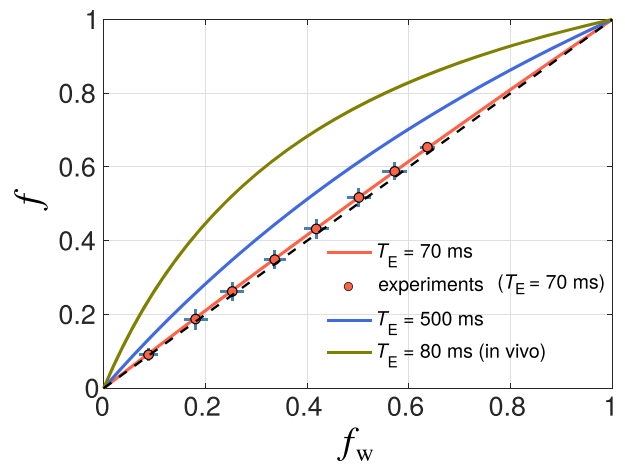


used to reproduce the situation of free water contamination encountered in the intra-tissue case. In the following subsections we discuss each of these features in the context of each phantom.

b. 'Is well characterised in terms of its microstructural properties'. Both phantoms were constructed with polyethylene fibres, which have been successfully used for the construction of several phantoms for DW MRI applications and have well known physical properties regarding water diffusion and relaxation.[50,51,54,55,61]

c. 'Is easy to assemble and reproducible'. Although the fibres were manually wound around the Perspex platforms, given the design and dimensions of the platforms (Figure 1) the assembly and reproducibility of both phantoms is relatively easy. However, higher levels of reproducibility, especially regarding fibre packing density, could potentially be achieved using a winding machine as in References 11 and 70

d. 'Is stable and non-toxic'. One of the advantages of artificial fibres such as polyethylene is that, given its hydrophobic properties, they are more stable than biological tissue or hydrophilic materials.[52,71] The phantoms presented in this work are constructed using only polyethylene fibres, Perspex platforms and distilled water. Therefore, the absence of any biological contamination can be guaranteed with the help of a preservative (eg NaN$_3$). In particular, our experiments span a time line of 564 days, and during this period our variability study did not show significant bias in the model parameter maps.

## 5.1 | Phantom 1

The diffusion-resolution phantom (Figure 1A) was conceived to investigate the CSF contamination and the elimination of the bias in diffusion models in voxels located at the CSF-tissue interface. The causes can be on the one hand random processes, such as the positioning of the imaging grid, and on the other hand characteristics relating to the dimensions of the object being imaged relative to the voxel size. The geometrical configuration of the phantom includes five sections of fibre bundles of different thicknesses separated by water and Perspex (noise) compartments of different sizes. We observed that DTIT$_2$ parameters were heavily affected by free water contamination in voxels located at the bulk-fibre interface, whereas FWET$_2$ parameters showed a more constant behaviour within each section of fibre bundles. This is clearly seen in the grey areas in the plotted profiles in Figure 2C and 2F. In particular, the leftmost section (2 mm thickness), which was almost invisible in the conventional FA, was completely recovered in FWET$_2$ FA. Moreover, a comparison of DTIT$_2$ and FWET$_2$ demonstrates that not only diffusion properties are affected by free water contamination, but also relaxation properties can be significantly altered. It should be noted that voxels presumed to be unaffected by PVE with free water, ie not positioned at the edge between the section of fibres and the bulk water, still show $f_w$ values between ~0.25 and ~0.35. This is most likely due to the presence of free water pockets formed by the imperfect packing of the fibre bundles. This, in turn, is a result of the fact that the fibre bundles (~700 single fibre strands) do not have a square cross-section (which would be required to have a perfect bundle packing), but rather have amorphous cross-sections. This feature can be seen in both single scan and reference truth maps.

These observations have important implications for in vivo DW MRI, given that CSF contamination is particularly crucial for some brain structures, such as the fornix, due to its small size and proximity to the ventricles.[13,14] In such cases CSF, contamination induces bias in DTI metrics that becomes a confounding macroscopic effect entangled with changes in the tissue microstructure, such as white matter atrophy.[13] Hence, the elimination of this bias becomes paramount. In this regard, our Phantom 1 could be utilized to optimize, among other things, the voxel size in order to minimize or eliminate CSF contamination in small structures.

The presence of thin sections of fibre bundles and small water compartments allows one to investigate more subtle processes leading to free water contamination. For instance, image distortions induced by eddy-currents depend on the direction of the field gradient. Therefore, a failure
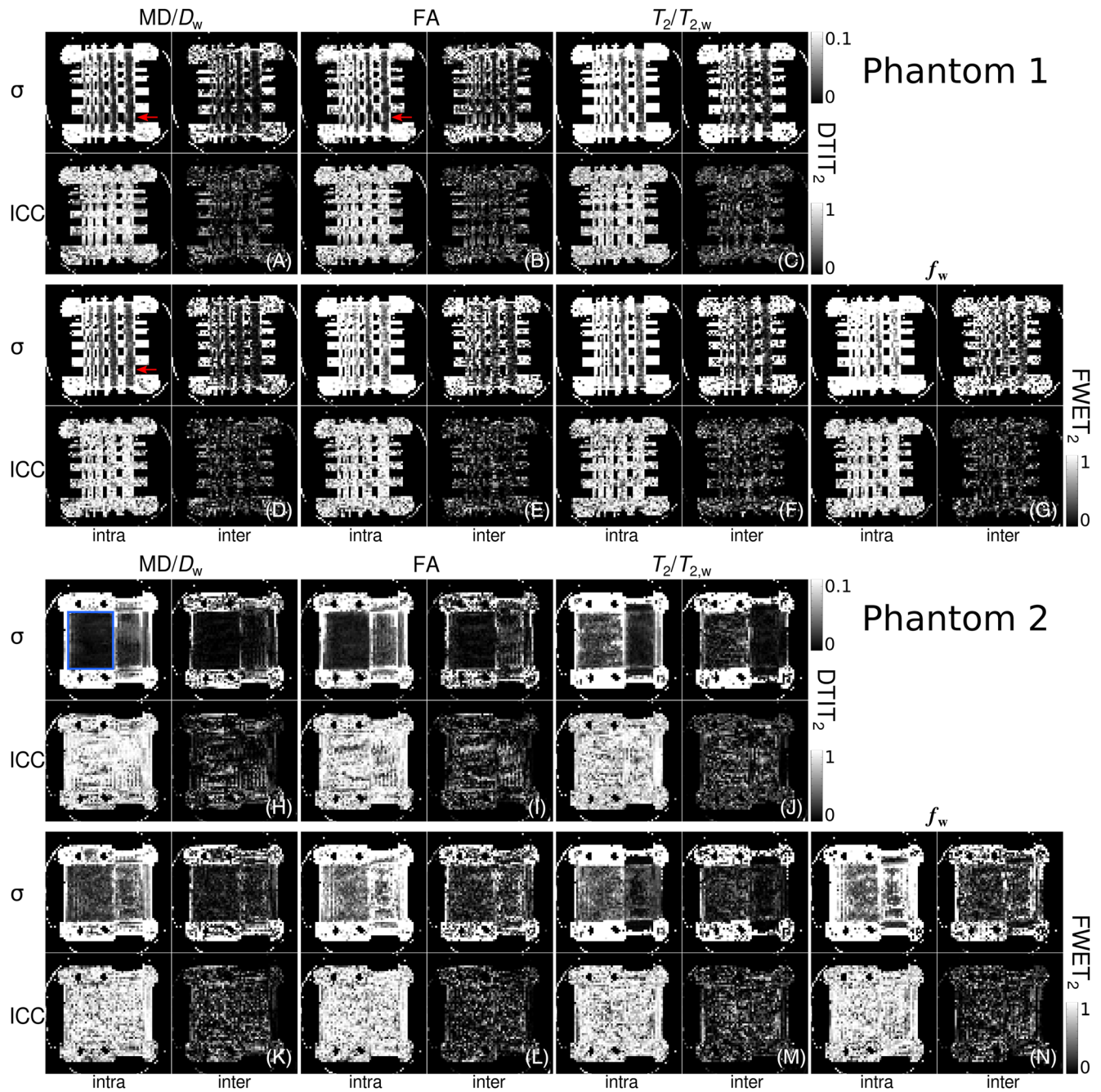
**FIGURE 7** A-C, H-J, DTIT$_2$ intra- and inter-site variability and ICC maps for MD/$D_w$ (A, H), FA (B, I) and $T_2$/$T_{2,w}$ (C, J) for phantom 1 (A-C) and phantom 2 (H-J). D-G, K-N, FWET$_2$ intra- and inter-site variability and ICC maps for MD/$D_w$ (D, K), FA (E, L), $T_2$/$T_{2,w}$ (F, M) and $f_w$ (G, N) for Phantom 1 (D-G) and phantom 2 (K-N). The framework used for the variability study is explained in detail in Appendix A

to fully correct these distortions will induce a small contamination dependent on the direction of the field gradient. Another case for which Phantom 1 is potentially useful is in the investigation of Gibbs ringing artefacts in DWI, which have been shown to strongly bias diffusion metrics in other models.[72] However, the study of such effects is beyond the aim of this work.

## 5.2 | Phantom 2

The previously introduced multi-section fibre phantom[50,73] includes a section that consists of parallel fibre bundles, conforming layers (Figure 1B), stacked in alternating directions. As a result, a free water compartment of variable volume is generated between the layers of fibres (volume increasing from left to right in Figure 1B). This feature results from the fact that each fibre bundle is made out of

approximately 700 single fibre strands, and therefore the thickness of each layer lies in the range from approximately 180 μm to 220 μm. This intra-bundle free water compartment mimics, although in a simplified manner, the situation encountered in intra-tissue free water contamination, in the sense that there are several free water compartments within a single voxel. We have assessed this feature using the $FWET_2$ model, which indeed shows that the relative free water fraction $f_w$ spans approximately the range [0.27,0.62] in the investigated slice (Figure 3). As a consequence of this increase in the size of the free water compartment, conventional $DTIT_2$ parameters show a strong free water contamination. For a given voxel in this phantom, $f_w$ is determined by the thickness of the fibre layers, the distance between the layers and their relation to the voxel dimensions (Figure 1B). The thickness of the layers and their separation are spatially variable and, as a consequence of this variation, $f_w$ is also spatially dependent. However, as the positioning of the imaging grid is random in nature and also influences the free water fraction, the values of $f_w$ cannot be a priori determined.

In Figure 3 we showed that MD, FA and $T_2$ from $DTIT_2$ show a spatial change that correlates with the estimated increase in the free water fraction. Yet the actual diffusion properties at the fibre compartment (ie estimated with $FWET_2$) also show a spatial change. Therefore, one can conclude that there is indeed a change in the fibre volume fraction at the fibre compartment, $\phi$, which directly affects the diffusion properties. Conversely, the transverse relaxation time of the fibre compartment did not show an observable change, which may be a consequence of the higher variance of this parameter compared with the diffusion parameters. This high variance is a result of the relatively short range of echo-times used in our experiments in relation to the long relaxation times.

We have taken advantage of the fact that we have also access to the PD in order to quantify the change in actual fibre volume fraction (Equation 8). Thus, analytical expressions for the diffusion properties in the fibre compartment, such as Equations B1-B3 (Appendix B), can be employed. Known theoretical models for the diffusion coefficient in binary systems are based on one of three approaches: obstruction effects,[74] free volume theory[75] and the hydrodynamic approach.[76] The applicability of these models was previously tested in binary solvent-polymer solutions and gels,[77] and was shown to hold in dilute systems or, in some experiments, at moderate concentrations. However, they were shown to break down for concentrated solutions. In the case of diffusion in the space between parallel cylinders, the Maxwell Garnett equation (Equation B1), which is independent of the fibre arrangement, only works well in the dilute regime. However, in our phantoms, the range of fibre volume fractions we observe falls into the concentrated regime, ie high packing density regime, observed in Figures 4 and 5. In such a range, the Maxwell Garnett equation fails to predict the observed behaviour (Figure 5). On the other hand, exact solutions for the whole range of fibre volume packing, based on the recursion relation proposed by Rayleigh,[78] can only be derived for regular arrays of cylinders, such as square (Equation B2) or hexagonal (Equation B3) arrangements.[79] However, Dyneema fibres are arranged in a random packing geometry, as previously observed using micro-CT.[51] This fact restrains an a priori derivation of the diffusion properties based on the geometrical configuration of the fibres.

Regarding the validity of the long-time approximation (Equations B1-B3), we observed that the root mean square (rms) displacement during the experiment, $l_t$, for the fibre compartment ranges from $l_t \approx 8$ μm (high $\phi$) to $l_t \approx 11$ μm (low $\phi$), calculated using an observation time of 70 ms. Similarly, one can calculate the structural length scale, $l_s$, based on the values of $\phi$,[52,80] to be of the order of $l_s \approx 5$ μm (high $\phi$) to $l_s \approx 6$ μm (low $\phi$). This means that molecules travel a distance of the same order as $l_s$ in both cases, and therefore the long-time limit is not fully developed. However, one can observe the expected trend. The transverse relaxation time at the fibre compartment, in contrast, showed almost no change across the phantom, which means that the change in $\phi$ is still not sufficiently large so as to induce significant changes.

The fact that the phantom shows different transverse relaxation times between the bulk and the fibre compartments ($T_{2,w} \approx 2.6$ s and $T_{2,t} \approx 0.7$ s) allowed us to investigate the $T_E$ dependence of the free water volume fraction as predicted by Equation 5. Thus, we exploited another of the benefits of $FWET_2$ by showing that, in that case, the free water fraction can be overestimated compared with the $T_E$-independent free water fraction. This overestimation was fairly small in our experiments due to the fact that $T_E$ in our DW experiments (70 ms) is small compared with the values of $T_{2,w}$ and $T_{2,t}$. However, the green line in Figure 6 demonstrates that the overestimation can potentially be much greater in in vivo experiments. Therefore, accounting for this effect becomes of paramount importance given the fact that several works in the literature have already shown $f$ to be a useful biomarker in the assessment of different brain conditions, such as Parkinson's disease,[30-32] Alzheimer's disease[29] or vasogenic oedema.[16] In all of these works, the difference in transverse relaxation was not taken into account. Another condition that could be assessed a priori using $FWET_2$ is traumatic brain injury, which has been shown to involve the formation of vasogenic oedema.[81,82]

## 5.3 | Reference truth maps and intra- and inter-site variability

With the purpose of constructing the reference truth maps, we first studied the variability of all $DTIT_2$ and $FWET_2$ maps in six scan sessions acquired at two different sites and with a time span of 564 days between the first and the last scan session. For the analysis of variability, we followed the framework published by Walker et al.[1] The first step of this framework consists in the detection of outliers using the distance from each scan session to the corresponding median calculated using all scan sessions. The median is a measure that, in contrast to the mean, is robust to outliers. Thus, in the case of a systematic difference, the presence of outliers produces only a small shift in the median value, allowing for easier

identification of outliers when looking at the difference between the median and each single map. We did not observe significant outliers in our results (Figure S1).

The analysis indicated that intra-site variability values were larger than inter-site ones for all model parameters. In an ideal situation, inter-site and intra-site variability values should be similar, indicating that there is no site bias and that the amount of variance is similar within each site and through all sites.[1] As a consequence, in an ideal case, $ICC_{intra} \approx ICC_{inter} \approx 0.5$. Conversely, one would expect greater $ICC_{inter}$ in cases where the mean value between sites differs, whereas $ICC_{intra}$ would be larger in those situations where the within-site variance differs between sites. The latter was the observed situation in our results for all ICC maps, ie $ICC_{intra} > ICC_{inter}$. Therefore, we conclude that the mean values between sites were rather similar (ie no site bias), which validates the framework we proposed for the construction of reference truth maps described previously.

The reference truth maps for all model parameters were constructed based on the former premise, using the median of all six scan sessions for each map. All reference truth maps were comparable to the corresponding single scan sessions (Figures 2–4). Moreover, we used the interquartile range (difference between the first and the third quartiles), which is also more robust to the presence of outliers than the standard deviation, to assess the voxel-wise uncertainty of the reference truth maps. As depicted in the corresponding profiles (Figures 2C, 2F, 3C, 3F, 4B and 4D), the uncertainty range for all parameters was within reasonable ranges.

## 5.4 | Other considerations

Regarding the pulse sequence, in this work we have used the paradigm of linear diffusion encoding originally proposed by Stejskal and Tanner.[83] However, more advanced diffusion encodings, such as double or triple diffusion encodings[84] or arbitrary $q$-trajectory encoding,[59,85] have been recently suggested and could potentially prove useful tools in the quest for free-water elimination and mapping.[86]

Concerning the fibre material for the construction of phantoms, an important issue requiring consideration is its magnetic susceptibility. Differences between the magnetic susceptibility of the fibres and the surrounding bulk liquid generate field gradients, which in turn produce image distortions due to the bias in the phase accumulated towards the end of the EPI readout. In the case of Dyneema fibres, the difference in magnetic susceptibility between the fibres and distilled water is ~1 ppm.[61] Yet, as observed in our results, this difference does not lead to appreciable image distortions, compared with the distortions that one normally observes in vivo induced by the presence of air, which has a difference in the magnetic susceptibility of nearly 8.5 ppm compared with tissue.[87]

## 5.5 | A brief, qualitative digression about exchange

One of the assumptions of FWE models is that water exchange between compartments is negligible. In this subsection we make some geometrical considerations of this situation.

In the case of Phantom 1, the rms displacement during the experiment for molecules in the bulk and fibre compartments is $l_w \approx 17$ μm and $l_t \approx 9$ μm (in the radial direction), respectively (using an observation time of 70 ms). During this time, only water molecules predominantly within distances $l_w$ (in the bulk compartment) and $l_t$ (in the fibre compartment) can reach the interface and exchange. A schematic representation of this
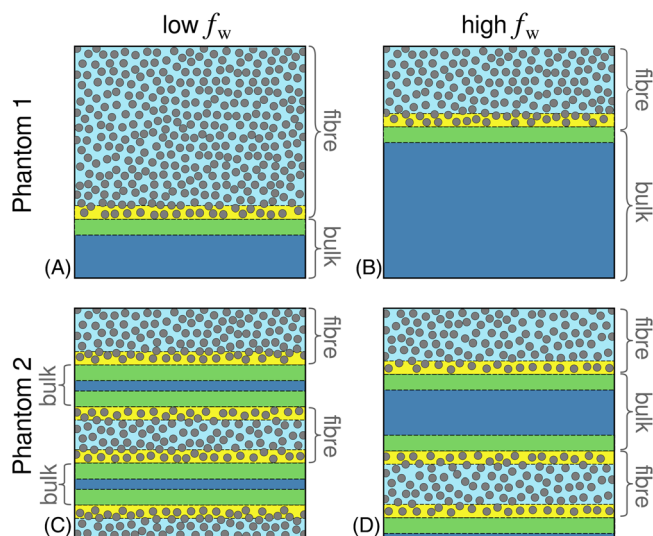


**FIGURE 8** Qualitative representation of the fraction of water molecules within a voxel that have the probability to exchange in the different configurations for phantom 1 (A, B) and phantom 2 (C, D). Note that the dimensions of fibres and shaded areas are qualitative

situation is shown in Figure 8. Green and yellow areas represent the layers with thicknesses $l_w$ and $l_t$, respectively. One can approximate the fractions of water molecules that have the possibility to exchange as the fractions located within these layers. For a voxel side length of 2 mm and assuming that the bulk-fibre interface is parallel to the voxel side, for example, one can demonstrate that these fractions are 14% (green area, Figure 8A) and 2% (green area, Figure 8B) for the bulk compartment with $f_w = 0.2$ and $f_w = 0.8$, respectively. In contrast, for the fibre compartment, these fractions are equal to 2% (yellow area, Figure 8A) and 4% (yellow area, Figure 8B) for $f_w = 0.2$ and $f_w = 0.8$, respectively. These estimates justify the slow-exchange limit in Phantom 1.

The situation with Phantom 2 is more complex since each voxel contains alternating layers of fibres and bulk water (Figure 8C and 8D). In this phantom, the rms displacement in the bulk compartments is $l_w \approx 18$ μm, whereas for the fibre compartment it ranges from $l_t \approx 8$ μm (high $\phi$, Figure 8C) to $l_t \approx 11$ μm (low $\phi$, Figure 8D). Conversely, the thickness of each layer of fibres was estimated to range from approximately 180 μm (high $\phi$) to 220 μm (low $\phi$), whereas the thicknesses of the bulk compartments ranged from approximately 80 μm (low $f_w$) to 200 μm (high $f_w$). Thus the fraction of water molecules that have the possibility of exchanging within the fibre compartments is 9% (yellow areas, Figure 8C) and 10% (yellow areas, Figure 8D), respectively. These fractions for the bulk compartments are 45% (green areas, Figure 8C) and 18% (green areas, Figure 8D), respectively. Therefore, based on this simplistic description, one can conclude that the effect of water exchange in Phantom 2 is a priori not negligible, especially in the region of high $\phi$ (low $f_w$).

For conventional DTI, an increase in the amount of exchange will cause an increase in bulk diffusivity and a decrease in FA. In the case of FWE models, it is expected to induce a bias in the estimation of $f_w$ and therefore in the tissue-specific diffusion tensor parameters.[16] Although water exchange has been extensively studied in the field of NMR,[88-90] open questions remain in relation to the exchange rate in the in vivo brain and its effect on the DW MRI metrics.[16,91-96] In particular, special care has to be taken with vasogenic oedema, given that tissue permeability plays an important role.[16] Thus we expect our Phantom 2 to become a useful tool for the design, validation and optimization of experimental techniques for the assessment of exchange.

# 6 | LIMITATIONS

A limitation of the current experimental setup of the phantoms is the long transverse relaxation times observed in the bulk and fibre compartments (2.53 s and 0.76 s, respectively), which are much larger than the values observed in the brain tissue (500 ms for CSF and an average of 60 ms for brain tissue at 3 T).[68,69] Therefore, in order to observe a clear difference between the $T_E$-dependent and $T_E$-independent free water fraction, one needs large $T_E$ values. Doping the water with $MgCl_2 \cdot 6H_2O$ (as in Reference 61 or with $CuSO_4$ in order to manipulate,[97] among other things, $T_2$, needs further investigation and is in our future plans. Another possibility is to use agarose gel, which has been shown to drastically reduce $T_2$.[98] However the construction process is challenging given that, due to the size of the agar chains, the solution barely fills the interstitial space via capillary force. One possibility requiring further investigation is the construction of the phantom while submerged in an agar bath. Regarding the fibre material, one possibility is to use hydrophilic materials, such as rayon,[52,55] which induce strong transverse relaxation as a result of surface interactions.

Although our Phantom 2 spans nearly 40% of the whole range of $f_w$, it still lacks the range [0,0.2], which is particularly important given that the free water fraction in the healthy, in vivo interstitial space is known to lie in this range.[99] This represents a limitation to our Phantom 2.

A limitation related to Dyneema fibres is that they are not hollow. Therefore, one can only mimic the water diffusion in the extra-cellular space. Other new materials though, which are able to reproduce both intra- and extra-cellular spaces,[46] could be used to construct phantoms with the same macroscopic characteristics as ours.

Regarding the estimation of the PD, a more exhaustive analysis should correct for the transmit field inhomogeneity and the receiver inhomogeneity separately, as demonstrated in several works in the field of quantitative water content mapping.[65,100,101]

# 7 | CONCLUSIONS

We have introduced the design and characterised the NMR properties of two artificial, anisotropic diffusion fibre phantoms useful for the investigation of FWE models. The first phantom was designed to mimic the case of free water contamination occurring via PVE in voxels at the CSF-tissue interface. The second phantom was used to reproduce the situation of free water contamination encountered in the intra-tissue case. Thus, investigation of FWE methods with such phantoms can be done on the basis of real experimental data. Moreover, the phantoms can be measured using clinical MRI scanners fitted with conventional receive coils.

We demonstrated the use of our phantoms to investigate the recently introduced FWE DTI model with explicit account of differences in the transverse relaxation times between compartments. Important diffusion and relaxation features, as well as the size of the free water compartment space, were captured by the $FWET_2$ model. Furthermore, we investigated the variability of different diffusion and transverse relaxation times in

six scan sessions at two different sites, which indicated a negligible site bias. Based on this, we constructed reference truth maps for each of the model parameters using the median of all six scan sessions.

Our phantoms are expected to be useful tools for the design and optimization of experimental protocols for FWE models as well as for the development and improvement of different data post-processing pipelines. Moreover, our phantoms represent useful systems for the validation and optimization of sequence-based approaches for FWE.

## ABBREVIATIONS

| | |
|---|---|
| ADC | apparent diffusion coefficient |
| CSF | cerebrospinal fluid |
| DTD | diffusion tensor distribution |
| DTI | diffusion tensor imaging |
| $DTIT_2$ | DTI with explicit $T_2$ attenuation |
| DW | diffusion weighted |
| FA | fractional anisotropy |
| FWE | free water elimination |
| $FWET_2$ | FWE model with explicit account of $T_2$ attenuation |
| $ICC_{inter}$ | inter-class correlation coefficient |
| $ICC_{intra}$ | intra-class correlation coefficient |
| MD | mean diffusivity |
| PD | proton density |
| PVE | partial volume effect |
| RD | radial diffusivity |
| rms | root mean square |
| ROI | region of interest |
| $T_2W$ | $T_2$ weighted |
| WLLS | weighted linear least squares |

## ORCID

*Ezequiel Farrher* https://orcid.org/0000-0003-2902-8667
*Farida Grinberg* https://orcid.org/0000-0001-8486-3126
*Li-Wei Kuo* https://orcid.org/0000-0002-0306-7329
*Kuan-Hung Cho* https://orcid.org/0000-0001-9267-8342
*Richard P. Buschbeck* https://orcid.org/0000-0001-8201-3937
*Ming-Jye Chen* https://orcid.org/0000-0003-0716-7156
*Husan-Han Chiang* https://orcid.org/0000-0003-0888-4149
*Chang-Hoon Choi* https://orcid.org/0000-0003-3569-0905
*N. Jon Shah* https://orcid.org/0000-0002-8151-6169

## REFERENCES

1. Walker L, Curry M, Nayak A, Lange N, Pierpaoli C. A framework for the analysis of phantom data in multicenter diffusion tensor imaging studies. *Hum Brain Mapp*. 2013; 34(10):2439-2454. https://doi.org/10.1002/hbm.22081
2. Johansen-Berg H, Behrens TEJ (Eds). *Diffusion MRI. From Quantitative Measurement to In-Vivo Neuroanatomy*. 2nd ed. Cambridge, Massachusetts, USA: Elsevier; 2014.
3. Lerner A, Mogensen MA, Kim PE, Shiroishi MS, Hwang DH, Law M. Clinical applications of diffusion tensor imaging. *World Neurosurg*. 2014;82(1):96-109. https://doi.org/10.1016/j.wneu.2013.07.083
4. Assaf Y. Can we use diffusion MRI as a bio-marker of neurodegenerative processes? *Bioessays*. 2008;30(11–12):1235-1245. https://doi.org/10.1002/bies.20851

5. De Belder FE, Oot AR, Van Hecke W, et al. Diffusion tensor imaging provides an insight into the microstructure of meningiomas, high-grade gliomas, and peritumoral edema. *J Comput Assist Tomogr*. 2012;36(5):577-582. https://journals.lww.com/jcat/Fulltext/2012/09000/Diffusion_Tensor_Imaging_Provides_an_Insight_Into.13.aspx

6. Sotak CH. The role of diffusion tensor imaging in the evaluation of ischemic brain injury—a review. *NMR Biomed*. 2002;15(7/8):561-569. https://doi.org/10.1002/nbm.786

7. Grinberg F, Farrher E, Ciobanu L, Geffroy F, Le Bihan D, Shah NJ. Non-Gaussian diffusion imaging for enhanced contrast of brain tissue affected by ischemic stroke. *PLoS ONE*. 2014;9(2):e89225. https://doi.org/10.1371/journal.pone.0089225

8. Mukherjee P, Miller JH, Shimony JS, et al. Diffusion-tensor MR imaging of gray and white matter development during normal human brain maturation. *Am J Neuroradiol*. 2002;23(9):1445-1456.

9. Kochunov P, Jahanshad N, Marcus D, et al. Heritability of fractional anisotropy in human white matter: a comparison of human Connectome project and ENIGMA-DTI data. *Neuroimage*. 2015;111:300-311. https://doi.org/10.1016/j.neuroimage.2015.02.050

10. Alexander AL, Hasan KM, Lazar M, Tsuruda JS, Parker DL. Analysis of partial volume effects in diffusion-tensor MRI. *Magn Reson Med*. 2001;45(5):770-780. https://doi.org/10.1002/mrm.1105

11. Bach M, Fritzsche KH, Stieltjes B, Laun FB. Investigation of resolution effects using a specialized diffusion tensor phantom. *Magn Reson Med*. 2014;71(3):1108-1116. https://doi.org/10.1002/mrm.24774

12. Pierpaoli C, Basser PJ. Toward a quantitative assessment of diffusion anisotropy. *Magn Reson Med*. 1996;36(6):893-906. https://doi.org/10.1002/mrm.1910360612

13. Metzler-Baddeley C, O'Sullivan MJ, Bells S, Pasternak O, Jones DK. How and how not to correct for CSF-contamination in diffusion MRI. *Neuroimage*. 2012;59(2):1394-1403. https://doi.org/10.1016/j.neuroimage.2011.08.043

14. Arkesteijn GAM, Poot DHJ, de Groot M, et al. CSF contamination-invariant statistics in conventional diffusion-weighted MRI of the fornix. *Biomed Phys Eng Express*. 2017;3(6):65003. https://stacks.iop.org/2057-1976/3/i=6/a=065003

15. Pierpaoli C, Jones DK. Removing CSF contamination in brain DT-MRIs by using a two-compartment tensor model. *Proc Int Soc Magn Reson Med*. 2004;21:1215.

16. Pasternak O, Sochen N, Gur Y, Intrator N, Assaf Y. Free water elimination and mapping from diffusion MRI. *Magn Reson Med*. 2009;62(3):717-730. https://doi.org/10.1002/mrm.22055

17. Papadakis NG, Martin KM, Mustafa MH, et al. Study of the effect of CSF suppression on white matter diffusion anisotropy mapping of healthy human brain. *Magn Reson Med*. 2002;48(2):394-398. https://doi.org/10.1002/mrm.10204

18. Baron CA, Beaulieu C. Acquisition strategy to reduce cerebrospinal fluid partial volume effects for improved DTI tractography. *Magn Reson Med*. 2015;73(3):1075-1084. https://doi.org/10.1002/mrm.25226

19. Vos SB, Jones DK, Viergever MA, Leemans A. Partial volume effect as a hidden covariate in DTI analyses. *Neuroimage*. 2011;55(4):1566-1576. https://doi.org/10.1016/j.neuroimage.2011.01.048

20. Jelescu IO, Veraart J, Fieremans E, Novikov DS. Degeneracy in model parameter estimation for multi-compartmental diffusion in neuronal tissue. *NMR Biomed*. 2016;29(1):33-47. https://doi.org/10.1002/nbm.3450

21. Hoy AR, Koay CG, Kecskemeti SR, Alexander AL. Optimization of a free water elimination two-compartment model for diffusion tensor imaging. *Neuroimage*. 2014;103:323-333. https://doi.org/10.1016/j.neuroimage.2014.09.053

22. Neto Henriques R, Rokem A, Garyfallidis E, St-Jean S, Peterson ET, Correia M. [Re] Optimization of a free water elimination two-compartment model for diffusion tensor imaging. *bioRxiv*. 2017. http://biorxiv.org/content/early/2017/02/15/108795.abstract.

23. Farrher E, Grinberg F, Abbas Z, Shah NJ. Free-water elimination in diffusion MRI: pushing the limits towards clinical applications. *Proc Int Soc Magn Reson Med*. 2017;25:3508.

24. Collier Q, Veraart J, Jeurissen B, den Dekker AJ, Sijbers J. Theoretical study of the free water elimination model. *Proc Int Soc Magn Reson Med*. 2015;2757.

25. Taquet M, Scherrer B, Boumal N, Peters JM, Macq B, Warfield SK. Improved fidelity of brain microstructure mapping from single-shell diffusion MRI. *Med Image Anal*. 2018;26(1):268-286. https://doi.org/10.1016/j.media.2015.10.004

26. Hoy AR, Kecskemeti SR, Alexander AL. Free water elimination diffusion tractography: a comparison with conventional and fluid-attenuated inversion recovery, diffusion tensor imaging acquisitions. *J Magn Reson Imaging*. 2015;42(6):1572-1581. https://doi.org/10.1002/jmri.24925

27. Albi A, Pasternak O, Minati L, et al. Free water elimination improves test-retest reproducibility of diffusion tensor imaging indices in the brain: a longitudinal multisite study of healthy elderly subjects. *Hum Brain Mapp*. 2017;38(1):12-26. https://doi.org/10.1002/hbm.23350

28. Maier-Hein KH, Westin C-F, Shenton ME, et al. Widespread white matter degeneration preceding the onset of dementia. *Alzheimer's Dement*. 2015;11(5):485-493.e2. https://doi.org/10.1016/j.jalz.2014.04.518

29. Hoy AR, Ly M, Carlsson CM, et al. Microstructural white matter alterations in preclinical Alzheimer's disease detected using free water elimination diffusion tensor imaging. *PLoS ONE*. 2017;12(3):1-21. https://doi.org/10.1371/journal.pone.0173982

30. Ofori E, Pasternak O, Planetta PJ, et al. Longitudinal changes in free-water within the substantia nigra of Parkinson's disease. *Brain*. 2015;138(8):2322-2331. https://doi.org/10.1093/brain/awv136

31. Ofori E, Pasternak O, Planetta PJ, et al. Increased free-water in the substantia nigra of Parkinson's disease: a single-site and multi-site study. *Neurobiol Aging*. 2015;36(2):1097-1104. https://doi.org/10.1016/j.neurobiolaging.2014.10.029

32. Planetta PJ, Ofori E, Pasternak O, et al. Free-water imaging in Parkinson's disease and atypical parkinsonism. *Brain*. 2016;139(2):495-508. https://doi.org/10.1093/brain/awv361

33. Bergmann Ø, Westin C-F, Pasternak O. Challenges in solving the two-compartment free-water diffusion MRI model. *Proc Int Soc Magn Reson Med*. 2016;24:0793.

34. Vallée E, Douaud G, Monsch AU, et al. Modelling free water in diffusion MRI. *Proc Int Soc Magn Reson Med*. 2015;23:0474.

35. Neto Henriques R, Bergmann Ø, Rokem A, Pasternak O, Morgado CM. Exploring the potentials and limitations of improved free-water elimination DTI techniques. *Proc Int Soc Magn Reson Med*. 2017;25:1787.

36. Collier Q, Veraart J, den Dekker AJ, Vanhevel F, Parizel PM, Sijbers J. Solving the free water elimination estimation problem by incorporating T2 relaxation properties. *Proc Int Soc Magn Reson Med*. 2017;25:1783.

37. van Dusschoten D, Dejager PA, Vanas H. Extracting diffusion constants from echo-time-dependent PFG NMR data using relaxation-time information. *J Magn Reson a*. 1995;116(1):22-28. https://doi.org/10.1006/jmra.1995.1185

38. van Dusschoten D. Unraveling diffusion constants in biological tissue by combining Carr-Purcell-Meiboom-gill imaging and pulsed field gradient NMR. *Magn Reson Med*. 1996;36(6):907-913. https://doi.org/10.1002/mrm.1910360613

39. Peled S, Cory DG, Raymond SA, Kirschner DA, Jolesz FA. Water diffusion, $T_2$, and compartmentation in frog sciatic nerve. *Magn Reson Med*. 1999; 42(5):911-918. https://doi.org/10.1002/(SICI)1522-2594(199911)42:5<911::AID-MRM11>3.0.CO;2-J

40. Galvosas P, Callaghan PT. Multi-dimensional inverse Laplace spectroscopy in the NMR of porous media. *C R Phys*. 2010;11(2):172-180. https://doi.org/10.1016/j.crhy.2010.06.014

41. Bernin D, Topgaard D. NMR diffusion and relaxation correlation methods: new insights in heterogeneous materials. *Curr Opin Colloid Interface Sci*. 2013;18(3):166-172. https://doi.org/10.1016/j.cocis.2013.03.007

42. Song Y-Q, Venkataramanan L, Kausik R, Heaton N. Chapter 4 Two-dimensional NMR of diffusion and relaxation. In: *Diffusion NMR of Confined Systems: Fluid Transport in Porous Solids and Heterogeneous Materials*. London, UK: Royal Society of Chemistry; 2017:111-155. https://doi.org/10.1039/9781782623779-00111

43. Jerome NP, d'Arcy JA, Feiweier T, et al. Extended T2-IVIM model for correction of TE dependence of pseudo-diffusion volume fraction in clinical diffusion-weighted magnetic resonance imaging. *Phys Med Biol*. 2016;61(24):N667. https://stacks.iop.org/0031-9155/61/i=24/a=N667

44. Holz M, Heil SR, Sacco A. Temperature-dependent self-diffusion coefficients of water and six selected molecular liquids for calibration in accurate $^1$H NMR PFG measurements. *Phys Chem Chem Phys*. 2000;2(20):4740-4742. https://doi.org/10.1039/b005319h

45. Wagner F, Laun FB, Kuder TA, et al. Temperature and concentration calibration of aqueous polyvinylpyrrolidone (PVP) solutions for isotropic diffusion MRI phantoms. *PLoS ONE*. 2017;12(6):e0179276. https://doi.org/10.1371/journal.pone.0179276

46. Fieremans E, Lee HH. Physical and numerical phantoms for the validation of brain microstructural MRI: a cookbook. *Neuroimage*. 2018;182:39-61.

47. Komlosh ME, Benjamini D, Barnett AS, et al. Anisotropic phantom to calibrate high-q diffusion MRI methods. *J Magn Reson*. 2017;275:19-28. https://doi.org/10.1016/j.jmr.2016.11.017

48. Fan Q, Nummenmaa A, Wichtmann B, et al. Validation of diffusion MRI estimates of compartment size and volume fraction in a biomimetic brain phantom using a human MRI scanner with 300 mT/m maximum gradient strength. *Neuroimage*. 2018;182:469-478.

49. Bucci M, Mandelli ML, Berman JI, et al. Quantifying diffusion MRI tractography of the corticospinal tract in brain tumors with deterministic and probabilistic methods. *NeuroImage Clin*. 2013;3:361-368. https://doi.org/10.1016/j.nicl.2013.08.008

50. Farrher E, Kaffanke J, Celik AA, Stöcker T, Grinberg F, Shah NJ. Novel multisection design of anisotropic diffusion phantoms. *Magn Reson Imaging*. 2012;30(4):518-526. https://doi.org/10.1016/j.mri.2011.12.012

51. Fieremans E, De Deene Y, Delputte S, et al. Simulation and experimental verification of the diffusion in an anisotropic fiber phantom. *J Magn Reson*. 2008;190(2):189-199. https://doi.org/10.1016/j.jmr.2007.10.014

52. Fieremans E, De Deene Y, Delputte S, Özdemir MS, Achten E, Lemahieu I. The design of anisotropic diffusion phantoms for the validation of diffusion weighted magnetic resonance imaging. *Phys Med Biol*. 2008;53(19):5405. http://stacks.iop.org/0031-9155/53/i=19/a=009

53. Grinberg F, Farrher E, Maximov II, Shah NJ. Complex patterns of non-Gaussian diffusion in artificial anisotropic tissue models. *Microporous Mesoporous Mater*. 2013;178:44-47. https://doi.org/10.1016/j.micromeso.2013.02.046

54. Reischauer C, Staempfli P, Jaermann T, Boesiger P. Construction of a temperature-controlled diffusion phantom for quality control of diffusion measurements. *J Magn Reson Imaging*. 2009;29(3):692-698. https://doi.org/10.1002/jmri.21665

55. Lorenz R, Bellemann EM, Hennig J, Il'yasov AK. Anisotropic phantoms for quantitative diffusion tensor imaging and fiber-tracking validation. *Appl Magn Reson*. 2008;33(4):419-429. https://doi.org/10.1007/s00723-008-0087-7

56. Nilsson M, Larsson J, Lundberg D, et al. Liquid crystal phantom for validation of microscopic diffusion anisotropy measurements on clinical MRI systems. *Magn Reson Med*. 2018;79(3):1817-1828. https://doi.org/10.1002/mrm.26814

57. Topgaard D. Multidimensional diffusion MRI. *J Magn Reson*. 2017;275:98-113. https://doi.org/10.1016/J.JMR.2016.12.007

58. De Almeida Martins JP, Topgaard D. Multidimensional correlation of nuclear relaxation rates and diffusion tensors for model-free investigations of heterogeneous anisotropic porous materials. *Sci Rep*. 2018;8:2488. https://doi.org/10.1038/s41598-018-19826-9

59. Westin C-F, Knutsson H, Pasternak O, et al. Q-space trajectory imaging for multidimensional diffusion MRI of the human brain. *Neuroimage*. 2016; 135:345-362. https://doi.org/10.1016/J.NEUROIMAGE.2016.02.039

60. Veraart J, Novikov DS, Fieremans E. TE dependent diffusion imaging (TEdDI) distinguishes between compartmental $T_2$ relaxation times. *Neuroimage*. 2018;182:360-369. https://doi.org/10.1016/j.neuroimage.2017.09.030

61. Farrher E, Lindemeyer J, Grinberg F, Oros-Peusquens A-M, Shah NJ. Concerning the matching of magnetic susceptibility differences for the compensation of background gradients in anisotropic diffusion fibre phantoms. *PLoS ONE*. 2017;12(5):1-20. https://doi.org/10.1371/journal.pone.0176192

62. Veraart J, Sijbers J, Sunaert S, Leemans A, Jeurissen B. Weighted linear least squares estimation of diffusion MRI parameters: strengths, limitations, and pitfalls. *Neuroimage*. 2013;81:335-346. https://doi.org/10.1016/j.neuroimage.2013.05.028

63. Grinberg F, Farrher E, Kaffanke J, Oros-Peusquens AM, Shah NJ. Non-Gaussian diffusion in human brain tissue at high *b*-factors as examined by a combined diffusion kurtosis and biexponential diffusion tensor analysis. *Neuroimage*. 2011;57(3):1087-1102.

64. Basser PJ, Pierpaoli C. Microstructural and physiological features of tissues elucidated by quantitative-diffusion-tensor MRI. *J Magn Reson B*. 1996; 111(3):209-219.

65. Abbas Z, Gras V, Möllenhoff K, Keil F, Oros-Peusquens A-M, Shah NJ. Analysis of proton-density bias corrections based on $T_1$ measurement for robust quantification of water content in the brain at 3 tesla. *Magn Reson Med*. 2014;72(6):1735-1745. https://doi.org/10.1002/mrm.25086

66. Jenkinson M, Smith S. A global optimisation method for robust affine registration of brain images. *Med Image Anal*. 2001;5(2):143-156. https://doi.org/10.1016/S1361-8415(01)00036-6

67. Jenkinson M, Bannister P, Brady M, Smith S. Improved optimization for the robust and accurate linear registration and motion correction of brain images. *Neuroimage*. 2002;17(2):825-841. https://doi.org/10.1006/nimg.2002.1132

68. Piechnik SK, Evans J, Bary LH, Wise RG, Jezzard P. Functional changes in CSF volume estimated using measurement of water $T_2$ relaxation. *Magn Reson Med*. 2009;61(3):579-586. https://doi.org/10.1002/mrm.21897

69. Gras V, Farrher E, Grinberg F, Shah NJ. Diffusion-weighted DESS protocol optimization for simultaneous mapping of the mean diffusivity, proton density and relaxation times at 3 tesla. *Magn Reson Med*. 2017;78(1):130-141. https://doi.org/10.1002/mrm.26353

70. Laun FB, Huff S, Stieltjes B. On the effects of dephasing due to local gradients in diffusion tensor imaging experiments: relevance for diffusion tensor imaging fiber phantoms. *Magn Reson Imaging*. 2009;27(4):541-548. https://doi.org/10.1016/j.mri.2008.08.011

71. Poupon C, Rieul B, Kezele I, Perrin M, Poupon F, Mangin J-F. New diffusion phantoms dedicated to the study and validation of high-angular-resolution diffusion imaging (HARDI) models. *Magn Reson Med*. 2008;60(6):1276-1283. https://doi.org/10.1002/mrm.21789

72. Perrone D, Aelterman J, Pižurica A, Jeurissen B, Philips W, Leemans A. The effect of Gibbs ringing artifacts on measures derived from diffusion MRI. *Neuroimage*. 2015;120:441-455. https://doi.org/10.1016/j.neuroimage.2015.06.068

73. Hubbard PL, Parker GJM. Validation of tractography. In: Johansen-Berg H, Behrens TEJ, eds. *Diffusion MRI*. 2nd ed. San Diego, CA: Academic; 2014:453–480. https://doi.org/10.1016/B978-0-12-396460-1.00020-2.

74. Lauffer RB. Paramagnetic metal complexes as water proton relaxation agents for NMR imaging: theory and design. *Chem Rev*. 1987;87(5):901-927. https://doi.org/10.1021/cr00081a003

75. Vrentas JS, Duda JL, Ling H-C. Free-volume theories for self-diffusion in polymer-solvent systems. I. Conceptual differences in theories. *J Polym Sci Polym Phys Ed*. 1985;23(2):275-288. https://doi.org/10.1002/pol.1985.180230204

76. Masaro L, Zhu XX. Physical models of diffusion for polymer solutions, gels and solids. *Prog Polym Sci*. 1999;24(5):731-775. https://doi.org/10.1016/S0079-6700(99)00016-7

77. Walderhaug H, Söderman O, Topgaard D. Self-diffusion in polymer systems studied by magnetic field-gradient spin-echo NMR methods. *Prog Nucl Magn Reson Spectrosc*. 2010;56(4):406-425. https://doi.org/10.1016/j.pnmrs.2010.04.002

78. Lord Rayleigh SRS. On the influence of obstacles arranged in rectangular order upon the properties of a medium. *Phil Mag*. 1892;34(211):481-502. https://doi.org/10.1080/14786449208620364

79. Perrins WT, McKenzie DR, McPhedran RC. Transport properties of regular arrays of cylinders. *Proc R Soc a*. 1979;369(1737):207-225. https://doi.org/10.1098/rspa.1979.0160

80. Zielinski LJ, Sen PN. Effects of finite-width pulses in the pulsed-field gradient measurement of the diffusion coefficient in connected porous media. *J Magn Reson*. 2003;165(1):153-161. https://doi.org/10.1016/S1090-7807(03)00248-9

81. Lu H, Lei X. The apparent diffusion coefficient does not reflect cytotoxic edema on the uninjured side after traumatic brain injury. *Neural Regen Res*. 2014;9(9):973-977. https://doi.org/10.4103/1673-5374.133150

82. Hergan K, Schaefer P, Sorensen A, Gonzalez R, Huisman T. Diffusion-weighted MRI in diffuse axonal injury of the brain. *Eur Radiol*. 2002;12(10):2536-2541. https://doi.org/10.1007/s00330-002-1333-2

83. Stejskal EO, Tanner JE. Spin diffusion measurements: spin echoes in the presence of a time-dependent field gradient. *J Chem Phys*. 1965;42(1):288.

84. Shemesh N, Jespersen SN, Alexander DC, et al. Conventions and nomenclature for double diffusion encoding NMR and MRI. *Magn Reson Med*. 2016;75(1):82-87. https://doi.org/10.1002/mrm.25901

85. Topgaard D. NMR methods for studying microscopic diffusion anisotropy. In: Valiullin R, ed. *Diffusion NMR of Confined Systems: Fluid Transport in Porous Solids and Heterogeneous Materials*. London, UK: New Developments in NMR. Royal Society of Chemistry; 2017:226–259. https://doi.org/10.1039/9781782623779.

86. Shemesh N, Özarslan E, Bar-Shir A, Basser PJ, Cohen Y. Observation of restricted diffusion in the presence of a free diffusion compartment: single- and double-PFG experiments. *J Magn Reson*. 2009;200(2):214-225. https://doi.org/10.1016/J.JMR.2009.07.005

87. Bakker CJG, de Roos R. Concerning the preparation and use of substances with a magnetic susceptibility equal to the magnetic susceptibility of air. *Magn Reson Med*. 2006;56(5):1107-1113. https://doi.org/10.1002/mrm.21069

88. Grinberg FA, Scirda VD, Fatkullin NF, Maklakov AI, Rogovina LZ, Storogyk IP. Diffusion spin echo decay by pulsed magnetic field gradient NMR and some structure features in blockcopolymer solutions. *Polym Bull*. 1985;14(3):355-359. https://doi.org/10.1007/BF00254960

89. Kärger J, Pfeifer H, Heink W. Principles and applications of self-diffusion measurements by nuclear magnetic resonance. In: Waugh J, ed. *Advances in Magnetic Resonance*. Vol.12 San Diego, CA: Academic; 1988:1-89.

90. Eriksson S, Elbing K, Söderman O, Lindkvist-Petersson K, Topgaard D, Lasič S. NMR quantification of diffusional exchange in cell suspensions with relaxation rate differences between intra and extracellular compartments. *PLoS ONE*. 2017;12(5):e0177273. https://doi.org/10.1371/journal.pone.0177273

91. Fieremans E, Novikov DS, Jensen JH, Helpern JA. Monte Carlo study of a two-compartment exchange model of diffusion. *NMR Biomed*. 2010;23(7):711-724. https://doi.org/10.1002/nbm.1577

92. Grinberg F, Farrher E, Oros-Peusquens A-M, Shah NJ. Random walks in model brain tissue. *AIP Conf Proc*. 2011;1330(1):31-34. https://doi.org/10.1063/1.3562226

93. Lasič S, Nilsson M, Lätt J, Ståhlberg F, Topgaard D. Apparent exchange rate mapping with diffusion MRI. *Magn Reson Med*. 2011;66(2):356-365. https://doi.org/10.1002/mrm.22782

94. Nilsson M, Lätt J, Van Westen D, et al. Noninvasive mapping of water diffusional exchange in the human brain using filter-exchange imaging. *Magn Reson Med*. 2013;69(6):1572-1580. https://doi.org/10.1002/mrm.24395

95. Schilling F, Ros S, Hu DE, et al. MRI measurements of reporter-mediated increases in transmembrane water exchange enable detection of a gene reporter. *Nat Biotechnol*. 2017;35(1):75-80. https://doi.org/10.1038/nbt.3714

96. Nilsson M, Van Westen D, Ståhlberg F, Sundgren PC, Lätt J. The role of tissue microstructure and water exchange in biophysical modelling of diffusion in white matter. *Magn Reson Mater Phys Biol Med*. 2013;26(4):345-370. https://doi.org/10.1007/s10334-013-0371-x

97. Van Geet AL, Hume DN. Measurement of proton relaxation times with a high resolution nuclear magnetic resonance spectrometer. *Direct Method Anal Chem*. 1965;37(8):983-988. https://doi.org/10.1021/ac60227a009

98. Mitchell MD, Kundel HL, Axel L, Joseph PM. Agarose as a tissue equivalent phantom material for NMR imaging. *Magn Reson Imaging*. 1986;4(3):263-266. https://doi.org/10.1016/0730-725X(86)91068-4

99. Ernst T, Kreis R, Ross BD. Absolute quantitation of water and metabolites in the human brain. I. Compartments and water. *J Magn Reson B*. 1993;102:1-8. https://doi.org/10.1006/jmrb.1993.1055

100. Neeb H, Ermer V, Stocker T, Shah NJ. Fast quantitative mapping of absolute water content with full brain coverage. *Neuroimage*. 2008;42(3):1094-1109. https://doi.org/10.1016/j.neuroimage.2008.03.060

101. Shah NJ, Zaitsev M, Steinhoff S, Zilles K. A new method for fast multislice $T_1$ mapping. *Neuroimage*. 2001;14(5):1175-1185. https://doi.org/10.1006/nimg.2001.0886

102. Maxwell Garnett JC. XII. Colours in metal glasses and in metallic films. *Phil Trans R Soc A*. 1904;203(359–371):385 LP-420. https://doi.org/10.1098/rsta.1904.0024

103. Kalnin JR, Kotomin E. Modified Maxwell-Garnett equation for the effective transport coefficients in inhomogeneous media. *J Phys a*. 1998;31(35):7227. http://stacks.iop.org/0305-4470/31/i=35/a=004

104. Sen PN, Basser PJ. Modeling diffusion in white matter in the brain: a composite porous medium. *Magn Reson Imaging*. 2005;23(2):215-220. https://doi.org/10.1016/j.mri.2004.11.014

105. Sen PN, Basser PJ. A model for diffusion in white matter in the brain. *Biophys J*. 2005;89(5):2927-2938. https://doi.org/10.1529/biophysj.105.063016

106. Jóhannesson H, Halle B. Solvent diffusion in ordered macrofluids: a stochastic simulation study of the obstruction effect. *J Chem Phys*. 1996;104:6807. https://doi.org/10.1063/1.471347

## SUPPORTING INFORMATION

Additional supporting information may be found online in the Supporting Information section at the end of this article.

## APPENDIX A: 7.1 | INTRA- AND INTER-SITE VARIABILITY

The framework proposed by Walker et al.[1] assumes that the experiments have been performed at $p = 1,...,P$ sites and $q = 1,...,Q_p$ time points. The first step of the analysis is based on the evaluation of the median of each model parameter $A$ through all time points at all sites. Outliers are then identified by subtracting the map at site $p$ and time point $q$, $A_{p,q}$, from the evaluated median. Significant deviations from the median are considered to be outliers.

The second step in the analysis consists in the evaluation of the intra-site and inter-site variances. Intra-site variance is assessed by first calculating the variance across all time points for each site and then calculating the mean of the variances. The intra-site variability is then given by the square root of the intra-site variance, ie

$$\sigma_{\text{intra}} = \left( \frac{1}{P} \sum_p \frac{1}{Q_p - 1} \sum_q \left( A_{p,q} - \langle A \rangle_p \right)^2 \right)^{1/2}. \tag{A1}$$

Inter-site variance is obtained by first evaluating the mean across all time points for each site and then evaluating the variance of the individual site means. The inter-site variability is written as

$$\sigma_{\text{inter}} = \left( \frac{1}{P-1} \sum_p \left( \langle A \rangle_p - \langle A \rangle \right)^2 \right)^{1/2}, \tag{A2}$$

where $\langle A \rangle_p = \sum_q A_{p,q} / Q_p$ is the site mean and $\langle A \rangle = \sum_p \langle A \rangle_p / P$ is the mean over all sites and time points.

We further evaluated the ICCs, defined as

$$\text{ICC}_{\text{intra}} = \frac{\sigma_{\text{intra}}^2}{\sigma_{\text{intra}}^2 + \sigma_{\text{inter}}^2} \tag{A3}$$

and

$$\text{ICC}_{\text{inter}} = \frac{\sigma_{\text{inter}}^2}{\sigma_{\text{intra}}^2 + \sigma_{\text{inter}}^2} \tag{A4}$$

respectively. These coefficients give the fraction of variance attributed to intra- and inter-site variability.

## APPENDIX B: 7.1 | FIBRE COMPARTMENT

Assuming a homogeneous distribution of perfectly aligned fibres within the fibre compartment and idealising the fibres as cylinders, the influence of the fibre volume fraction, $\phi$, on the radial diffusion coefficient in the long-time limit can be estimated analytically. In the dilute regime case, one can use the well known Maxwell Garnett equation,[102,103] which is valid for an arbitrary array of cylinders. The RD in this case can be written as the following:

$$D_{\perp,1}(\phi) = \frac{D_w}{1-\phi}\left(1 - \frac{2\phi}{1+\phi}\right). \tag{B1}$$

This approximation works well for fibre volume fractions up to $\phi \approx 0.4$. For higher packing densities, there are analytical solutions for the transport properties in regular arrays of cylinders, based on the recursion relation found by Lord Rayleigh for a square lattice[78] and later by Perrins et al[79] for a hexagonal lattice. These solutions were previously used in the formulation of an analytical model for the long-time diffusion coefficient in white matter by Sen and Basser.[104,105] We have adapted the solutions in References 104-106 for the case of solid fibres, which to third order are written as

$$D_{\perp,3}^{(s)}(\phi) = \frac{D_w}{1-\phi}\left[1 - 2\phi\left(1 + \phi - \frac{0.30583\phi^4}{1 - 1.40296\phi^8}\right)^{-1}\right] \tag{B2}$$

and

$$D_{\perp,3}^{(h)}(\phi) = \frac{D_w}{1-\phi}\left[1 - 2\phi\left(1 + \phi - \frac{0.07542\phi^6}{1 - 1.06028\phi^{12}}\right)^{-1}\right] \tag{B3}$$

for square (s) and hexagonal (h) lattices, respectively. Furthermore, FA can be written as $FA(\phi) = (1 - D_\perp(\phi)/D_w)/\sqrt{2D_\perp^2(\phi)/D_w^2 + 1}$, assuming that the eigenvalues of the diffusion tensor follow $D_w = \lambda_1 \geq \lambda_2 = \lambda_3$. Note that Equations B1-B3 are valid in the long-time limit.